Atomic-scale models for hardening in fcc solid solutions

L. Proville and S. Patinet
CEA, DEN, Service de Recherches de Métallurgie Physique, F-91191 Gif-sur-Yvette, France
(Received 26 May 2010; published 23 August 2010)

Atomic-scale simulations are associated with an elastic line model to analyze thoroughly the pinning strength experienced by an edge dislocation in some face-centered-cubic solid solutions, Al(Mg) and Ni(Al) with solute concentration comprise between 1 and 10 at. %. The one-dimensional elastic line model is developed to sketch out the details of the atomic scale. The account of such details is shown to yield a proper description of the dislocation statistics for the different systems. The quantitative departure between hardening in Al(Mg) and Ni(Al) is then demonstrated to hinge on the difference in the short-range interaction between the partial dislocations and the isolated impurities. It is also shown that an accurate description of the solid-solution hardening requires the account for the dislocation geometry and the dislocation interaction with clusters of solute atoms. The elastic line model allows us to perform some computations at the microscopic scales meanwhile accounting for the most important atomic details. A comparison with experimental data is attempted.

DOI: 10.1103/PhysRevB.82.054115 PACS number(s): 62.20.F−, 83.60.La

I. INTRODUCTION

The solid-solution hardening (SSH) of a metal stems from the pinning of its dislocations on the solute atoms introduced during material processing. The SSH depends essentially on the nature of the dislocation interaction with the impurities and the concentration of the latter. In order to estimate the stress threshold to which the dislocation depinning proceeds in face-centered-cubic (fcc) alloys, several statistical theories[1–5] were devised on the so-called *line tension model*, in which the dislocation is thought of as a one-dimensional (1D) elastic line dragged on a planar random landscape. From the different theoretical treatments applied to this model, the critical resolved shear stress (CRSS) required to liberate the dislocations was found to vary as the power law of the solute content, with an exponent η comprised between 1/2 and 1. The main differences between various theories arise from the assumptions made about the obstacle-dislocation interaction and about the typical roughness of the dislocation profile when the depinning proceeds. A number of studies contributes to the development of the 1D elastic line model (ELM) to tentatively release some of the rougher approximations introduced in the early SSH theories (see, for instance, Refs. 6–11).

Since SSH hinges on the pinning of dislocations in a crowd of atom-sized obstacles, the problem is worth being approach from the atomic scale. Employing the embedded atom method (EAM) (Refs. 12–14) to compute the interatomic forces in a nanocrystal, the dislocation depinning has already been simulated in a collection of binary alloys.[15–20] In dislocation theory, the main interest of such atomic-scale computations (ASCs) is to integrate the crystal deformation in the region near the dislocation core where the nonlinearity of the interatomic forces cannot be neglected. The EAM remains however an approximation and as such it presents some flaws varying with the system and that may be corrected by suitable developments as the bound order potentials (see, for instance, Ref. 21) or the modified EAM (see, for instance, Ref. 22).

The present work intends a quantitative comparison between the CRSS computed at the atomic scale and the CRSS predicted throughout ELM. The ASC are carried out in two different fcc alloys, Al(Mg) and Ni(Al) with the EAM developed by different authors.[15,23] The ELM is properly extended to sketch out the atomic details of the dislocation-obstacle interaction. In the early analytical theories for SSH, the dislocation pinning was resumed into the interaction of an elastic line with a single type of obstacle, which was regarded as an average obstacle. By contrast, we shows that in order to model quantitatively SSH in fcc alloys, the ELM must account thoroughly for the atomic details as (i) the dissociation of the dislocation core in two Shockley partials (see Fig. 1) due to the low stacking-fault energy (SFE) in (111) fcc crystal planes; (ii) the pinning force variation according to the solute atom position, above or below the glide plane; and (iii) the pinning by clusters of solute atoms in concentrated solid solutions.

In order to integrate the pertaining atomic details, a discrete version of the ELM has been developed. The discrete nature of this model allows us to describe the crystallography of the systems, thence sketching out the dislocation core structure as well as the dislocation-obstacle interaction for obstacles situated at various positions nearby the glide plane. The comparison between the depinning statistics computed

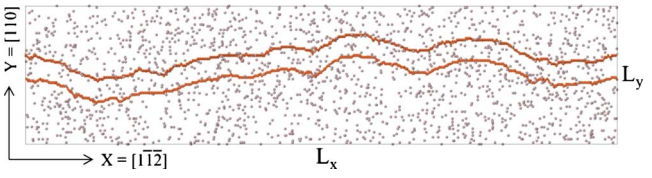

FIG. 1. (Color online) Plane view for an edge dislocation pinned by Mg solute atoms in Al(Mg) alloy, modeled within EAM (Ref. 23). The Mg atoms situated in the nearest planes that bound the (1$\bar{1}$1) glide plane are colored in gray while the atoms involved in the Shockley partial dislocations are colored in orange. The rest of the crystal atoms are not shown. The Mg concentration is $c_s = 2$ at. %.

independently from ASC and from ELM demonstrates that the latter is accurate enough to capture the main atomic-scale features of SSH. Interestingly, the ability in ELM for switching on or switching off selectively some of these features shows that the quantitative departure between hardening in Al(Mg) and Ni(Al) hinges on the difference in the short-range interaction between the partial dislocations and the isolated impurities. The same method allows us to determine how the solute atom clusters contribute to the dislocation pinning. Another important property of ELM, employed here, is that the integration of the small-scale details does not impede ELM working with large dimensions, i.e., of few micrometers, much larger than those afforded by ASC. The comparison of ELM predictions with the low-temperature experimental works performed by different authors[24] on Al(Mg) solid solutions demonstrates a satisfactory agreement.

The paper is organized as follows: in Sec. II, the ASC are described and our computations for the dislocation depinning in different model solid solutions are presented. In Sec. III, the ELM for the solution hardening in fcc alloys is introduced and its predictions for the depinning statistics are discussed in regard of the ASC in Secs. IV–VI. In Sec. VII, the ELM is eventually used to perform a multiscale study of dislocation static depinning. Our results are discussed in Sec. VIII.

II. ATOMIC-SCALE SIMULATIONS

A. Geometry of the simulation cell

In the ASC, the interatomic forces are modeled throughout the EAM developed previously by different authors.[13–15,23,25,26] The simulation cell (see Fig. 1) is oriented such as that the horizontal Z planes are the $(1\bar{1}1)$ planes of the fcc lattice. The edge dislocation Burgers vector $b=\frac{a_0}{2}[110]$ points at the glide direction, hereafter denoted as Y. The simulation box size along the directions $i=X,Y,Z$ is denoted by L_i. The periodic boundary conditions are applied along X and Y while the external applied stress τ is produced by imposing extra forces to the atoms in the upper and lower Z free surfaces.[19,27] In order to form a dislocation between the two $(1\bar{1}1)$ central midplanes, the displacement field of the elastic solution for a dislocation with Burgers vector b is applied to the atoms of the simulation box. The ASC are performed to minimize the total enthalpy under a fixed applied shear stress. The external applied stress is incremented by 0.3 MPa and for each increment the enthalpy minimization procedure is repeated until it either converges to a required precision (with interatomic forces inferior to 10^{-7} eV/Å) or until the dislocation has glided over a certain distance d_g, fixed later on. This procedure allows us to determine the static stress threshold associated with the dislocation depinning. The same method was employed in Refs. 17 and 20 with same notations but switching the axis label X and Y. The atoms involved into the dislocation core are identified by their first neighbor cells which differ from the perfect crystal.[27] In the simulations, the thermal effects are not present so the solute atom diffusion and the thermally activated glide are frozen. We thence work in an ideal case where the distribution of foreign atoms does not evolve and the dislocation glide occurs through a static depinning. Because of the rather low SFE of the (111) planes in fcc metals, the dislocation core dissociates in two Shockley partial dislocations (SPDs). Such a dissociation appears spontaneously in our enthalpy minimization procedure applied to ASC, as shown in Fig. 1.

B. Different solute random distributions

In order to decipher the statistics of the dislocation depinning in a fully three-dimensional (3D) random solid solution, we analyze different simplified situations. Four different types of solute atoms distributions are studied: (i) a single obstacle is introduced in the atomic simulation cell otherwise made of pure metal; (ii) the $(1\bar{1}1)$ planes situated just above the dislocation glide plane contains a random distribution of foreign atoms with an in-plane atomic concentration c_s; (iii) the two $(1\bar{1}1)$ planes that bound the glide plane contains a random distribution of foreign atoms with an atomic concentration c_s; and (iv) the solute atoms distribution is fully 3D. The ASC have been performed for the three types of constrained distributions and the fully random solid solution in both Al(Mg) and Ni(Al) alloys.

C. Single isolated obstacle

To analyze the elementary interaction between a dislocation and a single isolated solute atom at the atomic level, the simulations are carried out in a cell where only one atom of the pure crystal has been substituted with a foreign atom. Hereafter, such an isolated obstacle will be referred as to *type I* obstacle. The applied shear stress τ is incremented from zero to τ_m above which the dislocation liberates from the obstacle. Since the simulation cell is periodic along X, the obstacle and its periodic images form a regular array of obstacles separated by a distance L_x. The Peierls stress for the edge dislocation in the two pure fcc crystals was found negligible so the balance between the Peach-Koehler (PK) force and the obstacle pinning strength denoted by f_m leads to $f_m=\tau_m b L_x$. The maximum pinning force f_m has been computed for a single isolated impurity with different positions, i.e., above or below the glide plane, inside or outside the stacking-fault ribbon. The absolute values found for f_m are presented in Fig. 2(a) against the apical distance H to the glide plane. The same type of computations were performed for screw dislocations and confirmed an earlier study,[20] where it was found that both types of dislocations experienced similar pinning strengths. This similarity might be presented as a satisfactory explanation for the isotropy of the fcc alloy microstructure. The asymmetry of the obstacle strength f_m in tensile and compressive regions, i.e., above and below the glide plane is ascribed to the interatomic potentials anharmonicity. This asymmetry, well understood for edge dislocations which the deformation field changes in sign at the crossing of the glide plane, is also present in the case of screw dislocations, mainly because of the edge components of the partial dislocations. A precise comparison between the

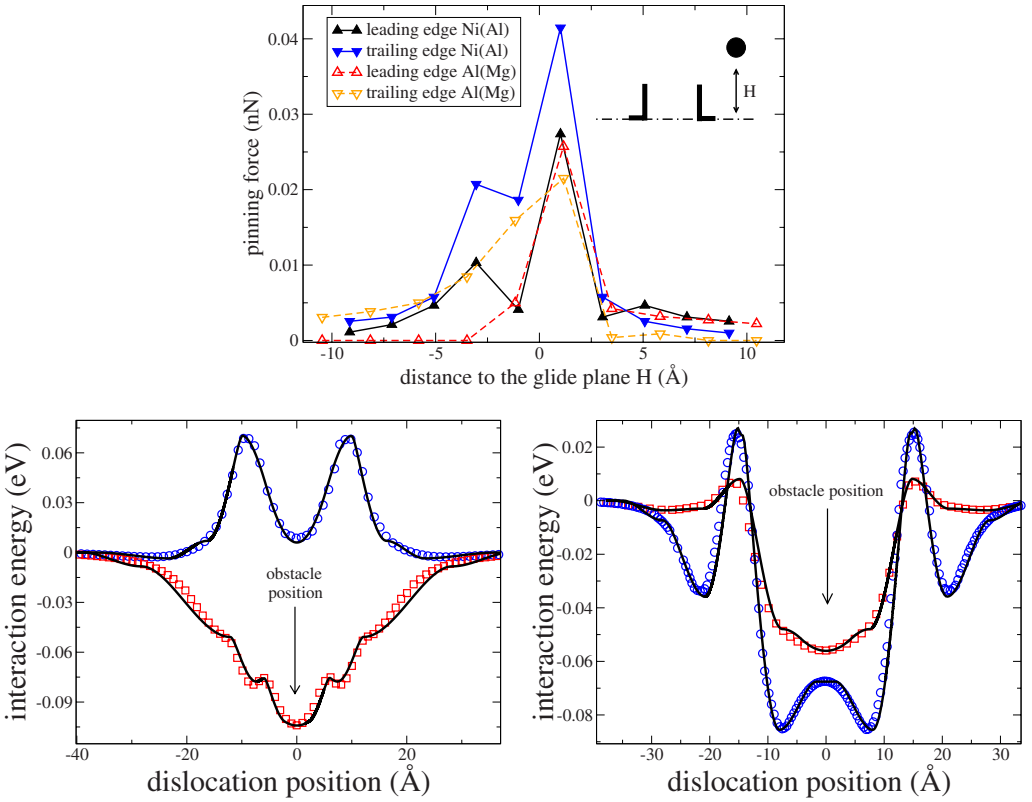

FIG. 2. (Color online) In (a), maximum pinning forces f_m (nanonewton) against the position of the solute atom with respect to the glide plane for every Shockley partial of the edge dislocation (leading: triangles up, trailing: triangles down) and for different systems: Al(Mg) (full symbols) and Ni(Al) (open symbols). Lines are guide to eyes. Underneath, internal energy of the simulation cells, U_{cell} against the position of the edge dislocation bypassing a solute atom: in (b) Mg in the Al crystal and in (c) Al in the Ni crystal. The different symbols correspond to the ASC realized as detailed in the text Sec. II [circles for the obstacles situated in the nearest $(1\bar{1}1)$ plane above the glide plane and squares for those in the nearest $(1\bar{1}1)$ plane below]. The continuous lines have been obtained from the adjustment of the 1D elastic line model presented in Sec. III.

different dislocation types is under progress.[28]

Once f_m has been computed for an obstacle situated at a certain position, we restart the simulation but with an external stress maintained to a constant value, slightly larger than τ_m. Then the variations in the internal energy U_{cell} of the simulation cells are analyzed during the dislocation bypassing. Such quantity is merely the sum of the interatomic EAM potentials over the whole simulation cell. After a steep drop of U_{cell}, over a few numerical steps, the internal energy U_{cell} varies smoothly. The rapid transient stage stems from the relaxation of the elastic displacement field imposed by the applied shear stress. The internal energy U_{cell} is recorded after the simulation cell has passed the rapid transient stage. We remarked that the use of a fast quench procedure to minimize the simulation cell enthalpy yields some jerky fluctuations of U_{cell}. A noiseless Langevin dynamics, with a suitably adjusted damping allowed us to record a continuous U_{cell} function against the ASC numerical increment, though the latter proved far much slower than a fast quench. In Figs. 2(b) and 2(c), the data for U_{cell} have been reported for the two different alloys, against the dislocation center of mass distance to the obstacle, for different positions of the latter, i.e., either in the nearest $(1\bar{1}1)$ plane above the glide plane or in the nearest $(1\bar{1}1)$ plane underneath. One clearly notices the nonmonotonous variations in the energy as the distance deviates from the energy maximum, in contrast to the predictions drawn from a first-order Volterra elastic theory.[29] This also contrasts with the assumptions made in an analytical model[2] for SSH. Such variations are particularly marked in Ni(Al) where up to six different extrema may be noticed for an obstacle situated just above the glide plane [see Fig. 2(c)]. The energy U_{cell} actually includes an elastic contribution stemming from the whole deformation of the crystal pieces, above and below the glide plane.[30] Though, under a constant external stress the energy variations associated with such an elastic deformation remain very small in comparison to the variations involved by the plastic deformation. The energy variations associated with the elastic deformation of the crystal will be discarded in our ELM analysis.

In Fig. 2(a), it is worth noticing that some pinning forces, corresponding to the obstacles situated in the next-nearest $(1\bar{1}1)$ planes that bound the glide plane are still appreciable in comparison to those associated with the nearest obstacles. In some cases, the strength of the former can even dominate those of the latter. In early SSH theories, a single average obstacle was regarded as a reasonable approximation. The confrontation of such an approximation with the results reported in Fig. 2 raises a question about how to define such an average.[20] This problem becomes increasingly complicate as

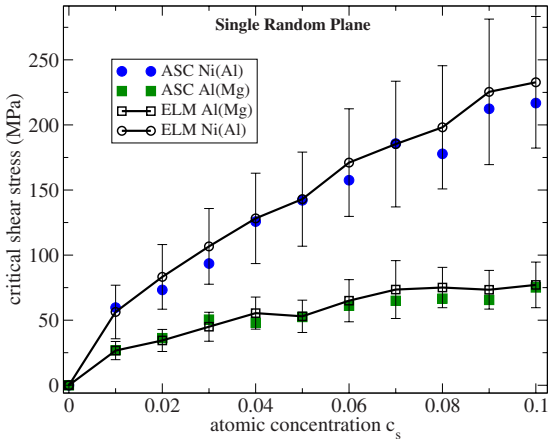

FIG. 3. (Color online) Critical resolved shear stress computed for Ni(Al) and Al(Mg) from the ASC (full symbols) for an edge dislocation passing through a crystal with a single $(1\bar{1}1)$ random plane situated just above the glide plane (referred as SRP in the text). The ELM predictions (open symbols with full lines) were obtained as detailed in Sec. III. The error bars corresponds to the mean square root of the ELM sampling.

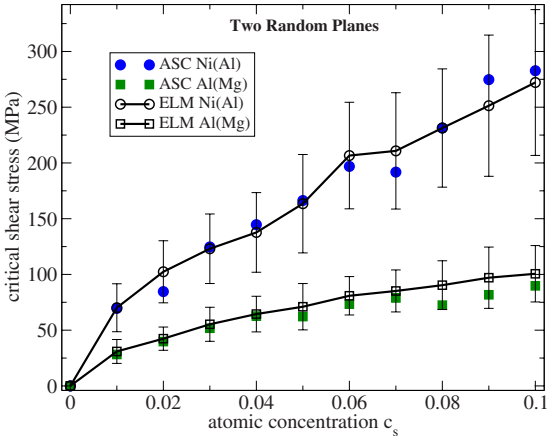

FIG. 4. (Color online) Same as in Fig. 3 but for different constrained solutions, referred as to TRP in the text, made of a pure crystal with solute atoms situated in the two contiguous planes that bound the dislocation glide plane. The corresponding ELM is detailed in Sec. III.

the solute concentration rises up to values where the pinning may result from the entanglement between the isolated obstacles and the solute atom dimers, or still even larger clusters.

D. Single random plane

The single random plane (SRP) distribution consists of a crystal made of the pure metal where the solute atom distribution is constrained in the only $(1\bar{1}1)$ plane situated just above the glide plane. To ease notations, the $(1\bar{1}1)$ crystal planes that bound the glide plane, above and below the glide plane, are denoted by $(A1)$ and $(B1)$, respectively. The next-nearest planes, above and below are denoted by Aj and Bj where $j=2$ for the second, $j=3$ for the third $(1\bar{1}1)$ planes, etc. The number of foreign atoms equals c_s times the number of atom sites in the (A1) plane. The ASC for SSH in SRP solid solutions are realized as described previously, by increasing adiabatically the applied stress τ. The dimensions of the simulation cell in X and Y directions are given in Ref. 31. The total course of the dislocation is here fixed to $d_g = 60$ Å. Once the dislocation has run over d_g the simulation is stopped. The value of τ required to reach d_g is averaged over a sampling of 20 different random distributions to determine the CRSS denoted by τ_c. Our results for τ_c against c_s have been reported in Fig. 3 for both systems. The CRSS is larger in the Ni(Al) SRP solutions than in the Al(Mg) ones. This agrees with the larger pinning strength f_m for the Al substitutional impurities in Ni, as seen from the comparison in Fig. 2(a). To understand how the data reported in Figs. 2(a)–2(c) might explain those reported in Fig. 3 a statistical model is required. This will be the purpose of the work reported in Sec. III.

E. Two contiguous random planes

The entanglement between the pinning forces from obstacles situated below and above the glide plane was discarded in the early analytical theories[1,2,4] for SSH. Different mixing laws were proposed depending on the strength of disorder.[32] To analyze how the pinning forces combine, a third type of distribution is employed. Instead of limiting the foreign atoms distribution in the $(A1)$ plane, the impurities can now also occupied the crystal sites situated below the glide plane, in the $(B1)$ plane. The edge dislocation statistics is then studied in such a solid solution, hereafter called a two random planes (TRPs) configuration. This study allows us to approach cautiously the realistic fully three-dimensional solid solution. The geometry of the simulation cell and the distribution sampling are the same as for the SRP solutions. The ASC results for the CRSS against c_s have been presented in Fig. 4. The comparison between the SRP (see Fig. 3) and the TRP solutions shows that the CRSS in the latter is slightly higher than the one found in the former. The entanglement of the obstacles situated above and below is not simply a linear superimposition of the pinning forces. The maximum applied stresses in TRP increase roughly by 20% in both Ni(Al) and Al(Mg) in comparison to the SRP in the same systems.

F. Fully random distribution

The ideal 3D solid solutions are formed by substituting some atoms of the pure crystal, randomly chosen, with solute atoms in the proportion fixed by c_s. The ASC for such fully random distributions (FRDs) integrate the contributions from solute atoms situated at different positions. The thermally activated solute diffusion being frozen in our static ASC, the dislocation is pinned by an ideal random distribution with a homogeneous solute concentration since no solute atoms atmosphere may form. The CRSS obtained in ASC for the edge dislocation depinning has been reported in Fig. 5. The comparison for the CRSS between FRD and previous other distributions shows that the main contribution to the dislocation pinning stems from the nearest crystal planes, namely, $(A1)$ and $(B1)$. The CRSS computed from ASC in TRP ap-

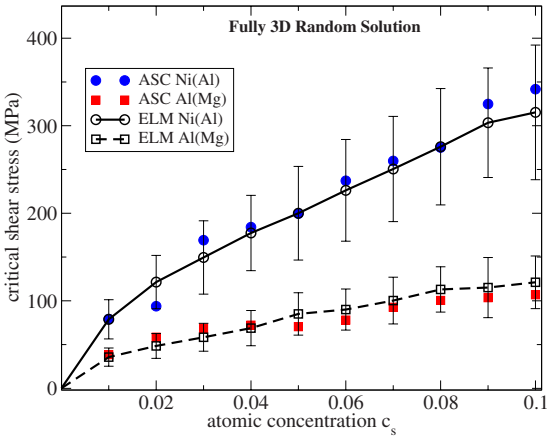

FIG. 5. (Color online) Same as in Figs. 3 and 4 but for fully random solid solutions (referred in the text as to FRD). The corresponding ELM is detailed in Sec. III.

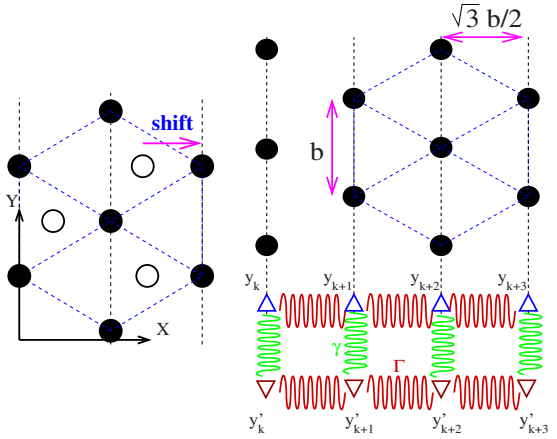

FIG. 6. (Color online) (a) Schematic representation of the transformation from the fcc crystal sites to a perfect hexagonal lattice. (b) Schematic representation for the one-dimensional ELM with two bound elastic lines. Circles represent the lattice sites and the triangles correspond to the nodes of discrete elastic lines. b stands for the norm of the Burgers vector (see Sec. II).

proach reasonably well those in FRD. As for SRP and TRP distributions, the dislocation pinning in Ni(Al) solutions proves much stronger than in Al(Mg), over the whole range of concentration. In order to determine to which extent our results could depend on the EAM employed in the ASC, we performed the same type of simulations but with some interatomic potentials different from those in use here. The comparison of SSH in the different atomic-scale models is presented in Appendix A where it is noted that the CRSS differ roughly of a factor 2 in the two systems. It seems therefore difficult to conclude about the precision of the EAM and a comparison with some experimental data is required. The Al(Mg) SSH will be the purpose of such a comparison in Sec. VII.

III. ELASTIC LINE MODEL

A. Harmonic spring ladder model

To analyze the CRSS against solute content in the different alloys, an extended version of the ELM is introduced. In its simplest version, the ELM requires[2,11] (i) a typical interaction potential between a single isolated obstacle and the dislocation and (ii) the dislocation stiffness, also named after *line tension*, and denoted as Γ. At the atomic scale, such parameters multiply[17,20] as each of them depends on the obstacle position with respect to the glide plane and which SPD is concerned, i.e., leading or trailing one. As remarked by Arsenault *et al.*,[9] the potential interaction never vanishes totally because of the Coulomb-type elastic stress field of the edge dislocation. It is then an interesting theoretical question whether it is reasonable to follow Nabarro[2] and introduce a distance cutoff over the interaction potential, without altering the CRSS computation.

To tackle the aforementioned difficulties, we develop the ELM model as follows: (i) to account for the multiplicity of the obstacles a discrete elastic line model is introduced; (ii) to sketch out the fcc crystal SPD in such a model, we consider two elastic lines bound by some elastic interactions; and (iii) to describe accurately the interaction potentials between the solute atoms and the SPD [see Figs. 2(b) and 2(c)] the elastic lines random potentials are constructed from the superimposition of some independent effective interaction potentials, adjusted on the ASC reported in Sec. II D. The method is now described thoroughly.

In order to account properly for the different atomic configurations of the nearest obstacles, a discrete version of the ELM (Ref. 33) must be introduced, allowing distinction between the crystal sites. In order to simplify the symmetries of the problem, we transform the fcc 3D perfect lattice into an hexagonal lattice as shown in Fig. 6(a). Our extended version for ELM is then depicted in Fig. 6(b) for the case of an edge dislocation. The dislocation is actually thought of as a ladder of harmonic springs, each linking some nodes [triangles in Fig. 6(b)] that are dragged along the rows of the perfect hexagonal lattice. The spring ladder represents the dislocation core dissociated in two SPD. Along the elastic lines, in X direction, the distance between two nearest rows is $b\sqrt{3}/2$ whereas in the Y direction it is $b/2$. To work with a dimensionless square lattice, we rescale the dimensions in X and Y directions with the associated inter-row distances. The dimensionless node position is denoted as y_k for the leading chain and y'_k for the trailing one. The PK force stemming from the applied shear stress applies equally on each dislocation segment. The PK force applied to a segment of length $\sqrt{3}b/2$ is reported totally on the nearest nodes. The overdamped Langevin equation for the chain node k of the leading chain writes as follows:

$$\lambda \dot{y}_k = \frac{\Gamma}{\sqrt{3}}\Delta_k y_k - \gamma[y_k - y'_k - d^*] + \tau s - \sum_{i,j} V'_{I-j}(y_k - a_{k,i,j}), \tag{1}$$

where λ is a damping coefficient with no physical importance in our static computations, $s=\sqrt{3}b^2/4$ is the unit area of our hexagonal lattice, Δ_k the discrete Laplacian, d^* is the equilibrium distance between the SPD, Γ and γ are the spring constants, $a_{k,i,j}$ is the coordinate of the ith obstacle in

the kth row of the plane labeled $j \in [(An),(Bn)]$ with $n \in \mathbb{N}$ and $V_{I-j}(x)$ is the interaction potential between a chain node and the type I obstacle situated in plane j. The same equation holds for y_k' but switching the sign of γ and replacing the interaction potential V_{I-j} with the appropriate form associated with the trailing partial, and denoted as W_{I-j}. In Appendix B, Eq. (1) is derived from the continuous model for a 1D elastic line, also known as the *line tension model*. The Coulomb-type interactions between the segments of a given partial are neglected in the present approach. The two chains are bound together with harmonic springs that intend to represent the SPD interactions. The strength of these springs is obtained from the SPD interaction force per unit length, derived from the dislocation elastic theory:[34] $F_s = \gamma_I - \alpha\mu b^2/2\pi r$, where γ_I is the SFE per unit area, r is the dissociation width, and α is a geometric factor varying with Poisson's ratio ν and with the true direction of the SPD Burgers vectors. For some perfect SPD,[34] $\alpha = [1/(1-\nu) - 1/3]/4$ which gives approximately $\alpha \approx 0.3$ in Al and $\alpha \approx 0.26$ in Ni if one uses for Poisson's ratio $\nu_{\mathrm{Al}} = 0.347$ and $\nu_{\mathrm{Ni}} = 0.28$. The other physical constants needed here are the $(1\bar{1}1)$ shear modulus $\mu = (C_{11} - C_{12} + C_{44})/3$ which gives $\mu_{\mathrm{Al}} = 30\,833$ Mpa and $\mu_{\mathrm{Ni}} = 74\,600$ MPa and the norm of the dislocation Burgers vector $b = a_0/\sqrt{2}$ with $a_0 = 4.031$ Å in Al and $a_0 = 3.52$ Å in Ni.

Because of the limited dimensions of ASC, the elastic interactions between the SPD and their periodic images along the Y direction must be accounted for, which leads, for the leading partial to a force per unit length,

$$F_s(r) = \gamma_I - \alpha\frac{\mu b^2}{2\pi}\left[\frac{1}{r} + \sum_{j\geq 1} -\frac{1}{(jL_y) - r} + \frac{1}{(jL_y) + r}\right]. \quad (2)$$

This equation can be reduced using a well-known identity of the Riemann zeta function,

$$F_s(r) = \gamma_I - \alpha\frac{\mu b^2}{2L_y}\left[\cot\left(\frac{\pi r}{L_y}\right)\right]. \quad (3)$$

According to the previous elastic theory applied to our atomistic simulation cell, the equilibrium distance between SPD would then be

$$d_{\mathrm{SPD}} = \frac{L_y}{\pi}\arctan\left(\frac{\alpha\mu b^2}{2L_y\gamma_I}\right). \quad (4)$$

In Eq. (1), the dimensionless separation distance between SPD has been denoted by $d^* = 2d_{\mathrm{SPD}}/b$. For very large L_y in comparison with $d_0 = (\frac{\alpha\mu b^2}{2\pi\gamma_I})$, the width of the stacking fault ribbon tends to d_0 as expected in an infinite media.[34] Through ASC, both d_{SPD} and the stacking-fault energy γ_I can be computed independently in pure Ni and pure Al. The former is simply obtained from simulations with a dislocation in the computational cell as presented in Sec. II while the latter is obtained by construction of another simulation cell[35,36] with three periodic boundary conditions allowing to produce some perfect stacking faults, i.e., not bounded by dislocations. In Ni, we found $\gamma_I = 89$ mJ/m^2 whereas in Al $\gamma_I = 109$ mJ/m^2. The SFE computed within the present EAM underestimate the experimental estimations found by Carter and Holmes[37] in Ni and Westmacott and Peck[38] in Al, with $\gamma_I = 120-130$ mJ/m^2 and $\gamma_I = 120-144$ mJ/m^2, respectively. Using the same computational method as in Sec. II with no external shear stress applied, the dissociation distance is computed in ASC. For a simulation cell with dimensions given in Ref. 31, it is found that $d_{\mathrm{SPD}} = 28.6$ Å in Ni and $d_{\mathrm{SPD}} = 17.1$ Å in Al. To render the ASC for d_{SPD} compatible with those for γ_I through the elastic theory Eq. (4) we must adjust the dimensionless coefficient α to $\alpha = 0.462$ in Ni and $\alpha = 0.503$ in Al.

The variation in the SFE with solute concentration may be important in FRD solid solutions. The SFE has been computed for solid solutions as for the pure metals but introducing randomly the impurities in the simulation cell as in Sec. II F. The SFE is found to decrease linearly with the solute content c_s,

$$\gamma_I = 89c_s - 670c_s \text{ in Ni(Al)}$$

and

$$\gamma_I = 109c_s - 249c_s \text{ in Al(Mg)} \quad (5)$$

with numerical coefficients unit in millijoule per square meter. The steepest decrease is noticed for Ni(Al). The ASC presented in Sec. II F also allowed us to compute the average distance between SPD, d_{SPD} for a finite concentration with no applied stress. While d_{SPD} hardly varies with c_s in Al(Mg), its variation is much more pronounced in Ni(Al). The analytical computations for d_{SPD} in Eq. (4), where γ_I is given by Eq. (5) provides us a satisfactory approximation for d_{SPD} in comparison to ASC in Ni(Al). The coefficient α in Eq. (4) has been adjusted only to fit the ASC data for $c_s = 0$ meanwhile for finite c_s it was not required to change the value fixed at $c_s = 0$. In Al(Mg) the same analytical treatment overestimates our ASC data. Consequently, in the following ELM computations d_{SPD} will be invariant against c_s in the case of Al(Mg) whereas in Ni(Al) we shall employ Eq. (4) combined with Eq. (5) to fix d_{SPD}, and subsequently d^* in Eq. (1). The ASC performed with SRP and TRP constrained solid solutions (see Secs. II D and II E) showed us that the stacking-fault ribbon width depends marginally on the solute content in both alloys. Such variations will then be discarded when the ELM computations will concern these constrained solid solutions.

The first-order expansion of F_s in Eq. (3), around the equilibrium distance d_{SPD} yields a linear force proportional to $(r - d_{\mathrm{SPD}})$,

$$F_s(r) = -\frac{\alpha\pi\mu b^2}{2L_y^2\sin\left(\frac{\pi d_{\mathrm{SPD}}}{L_y}\right)^2}(r - d_{\mathrm{SPD}}). \quad (6)$$

Multiplying F_s by the unit area of our dimensionless lattice $s = \sqrt{3}b^2/4$, we obtain the spring constant γ of the transversal springs in the elastic ladder presented in Fig. 6(b),

$$\gamma = \frac{\alpha \pi \mu s b^2}{2L_y^2 \sin\left(\frac{\pi d_{\mathrm{SPD}}}{L_y}\right)^2}. \quad (7)$$

Although the interdislocation forces are usually presented as long-range elastic Coulomb-type forces, the transversal springs in the ELM link only the nodes that are situated in the same lattice row, along the Y direction. We acknowledge that this may be thought of as a rather rough approximation which the reliability is yet supported by the following analysis for the profile of anchored dislocations. The study of such profiles also allows us to determine the strength Γ associated with the lateral springs in the elastic ladder.

Some ASC with a single foreign atom are realized as described in Sec. II C. The dislocation is then anchored by an isolated obstacle and it takes different profile according to the external shear stress inferior to the critical value. In order to span a wide range of stress and thus to gain in precision on the computation of the dislocation bowing, the foreign atom is substituted with a fictitious atom, which the first-neighbor bonds are artificially maintained invariant during the simulation, such that the dislocation cannot pass the obstacle (unless the stress attains the Orowan threshold which is out of purpose here). In Figs. 7(a) and 7(b), the profiles of the dislocation computed from ASC have been reported for different applied stresses. The triangles represent the position of each dislocation segment in the ASC. The different configurations were obtained for an obstacle situated in (A1) plane, in front of the leading partial in Al [Fig. 7(a)] and in front of the trailing partial, in the stacking-fault ribbon in Ni [Fig. 7(b)]. In order to reproduce such computations within the ELM, we introduce also a fictitious obstacle like in ASC, with an arbitrary form for the potentials V_{I-j} and W_{I-j}, sufficiently hard to impede the passage of the elastic ladder. Then we proceed the same as in ASC to determine the configuration of the elastic ladder under the same applied stress. The elastic ladder profiles in ELM eventually can be compared to the ASC as done in Figs. 7(a) and 7(b) where the profiles of the elastic ladders are represented by continuous lines. The adjustment of the spring constant Γ in the ELM was realized such that we found similar anchored profiles in both ELM and ASC. The comparisons were performed for different length L_x and different external stresses τ. The adjustment of Γ, obtained for a set of parameters L_x and τ proves to be valid over a broad range of those parameters.

Throughout such an adjustment, we found $\Gamma_{\mathrm{Al}} = 0.101$ nN and $\Gamma_{\mathrm{Ni}} = 0.162$ nN. According to the analytical elastic theory[39] for an edge dislocation, the line tension can be estimated with the formula,

$$\Gamma^{\mathrm{el}} = \mu b^2 \frac{1-2\nu}{4\pi(1-\nu)} \ln(R/b), \quad (8)$$

where R corresponds to the outer cutoff of the elastic theory. In our simulation cell, R would correspond to $L_z/2$, i.e., the shortest distance between the dislocation and the free surfaces of the cell. With L_z in Ref. 31, Eq. (8) yields $\Gamma^{\mathrm{el}}_{\mathrm{Al}} = 0.2$ nN and $\Gamma^{\mathrm{el}}_{\mathrm{Ni}} = 0.5$ nN. The discrepancy between Eq. (8) and our computations is partly due to the fact that Eq. (8) applies to a dislocation that is not dissociated whereas in our problem the coefficient Γ concerns the stiffness of a single SPD. To tentatively reduce the discrepancy, we apply the general formula from the dislocation elastic theory[39] to the case of a single partial dislocation,

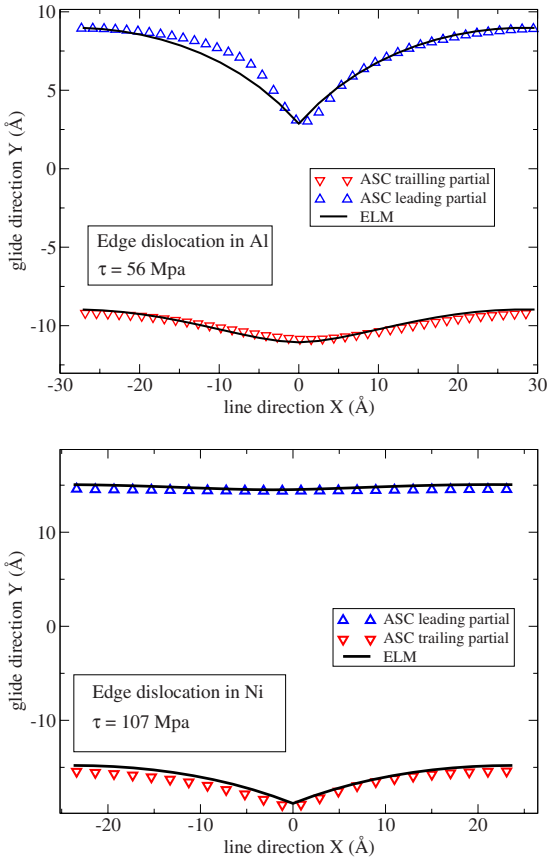

FIG. 7. (Color online) Configuration for an edge dislocation, anchored on an arbitrary strong obstacle situated either in front of the trailing partial (a) or in between both partials (b), in a crystal of Al (a) and in a crystal of Ni (b) for different applied shear stresses (see insets). The triangles represent the dislocation segments computed within atomic-scale simulations and the continuous lines correspond to the results from the elastic line model presented in Fig. 6(b).

$$\Gamma^{\mathrm{el}} = \frac{\mu b_p^2[(1+\nu)\cos^2(\beta) + (1-2\nu)\sin^2(\beta)]}{4\pi(1-\nu)} \ln(R/b), \quad (9)$$

where this time, $b_p = a_0/\sqrt{6}$ stands for the norm of the partial burgers vector while $\beta \in [\pi/3, 2\pi/3]$ is the angle between the line direction and the burgers vector of either the leading or the trailing partials. Equation (9) yields $\Gamma^{\mathrm{el}}_{\mathrm{Al}} = 0.132$ nN and $\Gamma^{\mathrm{el}}_{\mathrm{Ni}} = 0.25$ nN which proves closer from our computations in both systems though it still overestimates it. Actually applying Eq. (9) to SPD still corresponds to a quite rough approximation where the SPD are considered as some isolated dislocations which is by far not realistic since the SPD are in contact with a stacking fault. Nevertheless the comparison with the elastic theory of dislocation allowed us to confirm the order of magnitude of Γ.

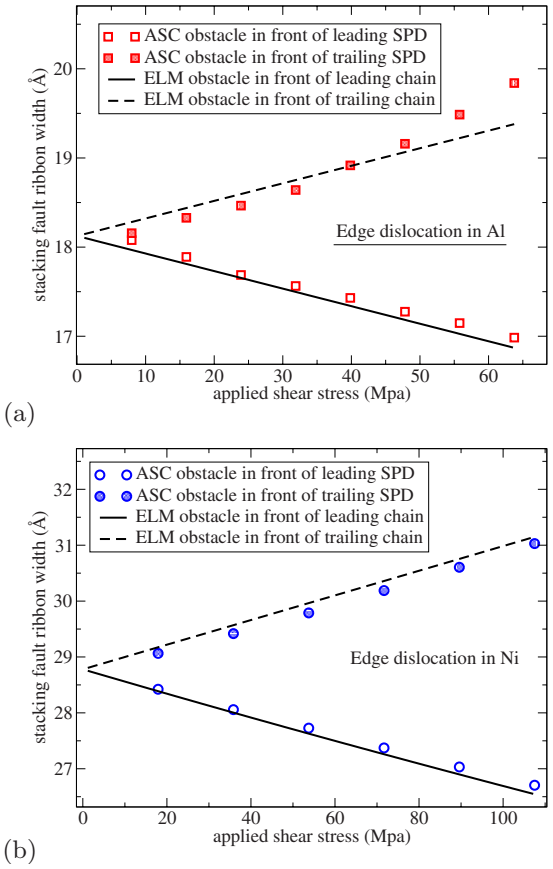

FIG. 8. (Color online) Width of the stacking fault ribbon d_{SPD} for an edge dislocation anchored on an arbitrary strong obstacle situated either in front of the trailing partial or in between both partials, in a crystal of Al (a) and in a crystal of Ni (b). The symbols represent the computations from atomic-scale simulations and the lines correspond to the elastic line model presented in Figs. 6(a) and 6(b) with the same geometric parameters given in Ref. 31.

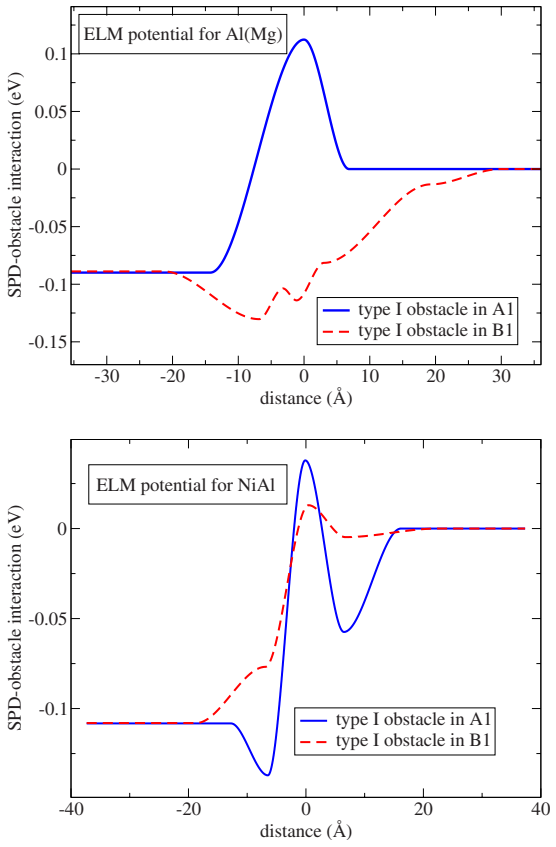

FIG. 9. (Color online) Interaction potentials V_{I-j} between the elastic line corresponding to the leading partial, for different systems and different positions of the obstacle above ($A1$) and below ($B1$) the glide plane. These potentials have been constructed with a series of cubic polynomials, interpolating the coordinates for the first derivative zeroes.

In order to test further our harmonic spring ladder model, we determine the variation in the separation distance d_{SPD} between anchored partial dislocations against the applied stress. The ASC data have been presented for both alloys in Figs. 8(a) and 8(b) with symbols. Depending on the position of the obstacle, i.e., outside or inside the stacking-fault ribbon, the distance d_{SPD} either decreases or increases with τ, respectively. Once again, the same type of computations performed within the ELM [see lines in Figs. 8(a) and 8(b)] demonstrates a satisfactory agreement with ASC.

From the previous comparisons, we estimate that the elastic properties of the dissociated dislocation have been successfully captured within the spring chain ladder. The short-range harmonic interaction between the chain nodes allows us to avoid the computational load that would imply the numerical treatment of the long-range Coulomb-type interactions. It is worth noticing that the latter however enter effectively into the determination of the spring constant Γ and γ since these ELM parameters are adjusted to fit the ASC where the long-range elastic effects are present.

B. Isolated solute atoms pinning potentials

In the ELM, we assume that the obstacle forces apply solely on the ladder nodes in the lattice row where is situated the obstacle. The interaction potentials V_{I-j} and W_{I-j} between the obstacles and the elastic ladder nodes are constructed with a series of cubic polynomials, interpolating the zeroes of the potential-energy derivatives. The position of such zeroes and the values taken by the potential energy at such points serve as adjustable variables. The coefficients of the polynomials are determined consistently by the conditions of continuity of the potential and its first derivative. The adjustable variables are tuned such that to sketch out the internal energy U_{cell} between the partial dislocations and the foreign atoms, in the ASC presented in Sec. II D. In Figs. 9(a) and 9(b), the end results from our spline procedure is presented for the two systems and for the interaction potential between the leading partial and an isolated obstacle either situated in the ($A1$) plane (full line) or in the ($B1$) plane (dashed line). The same procedure has been applied to derive the interaction potential with the trailing partial. The total energy associated with Eq. (1) is simply given by

$$E_{\mathrm{ELM}} = \frac{b}{2}\sum_{k}\left\{\frac{\Gamma}{2\sqrt{3}}[(y_k - y_{k-1})^2 + (y'_k - y'_{k-1})^2] + \frac{\gamma}{2}(y_k - y'_k - d^*)^2 + \sum_{i,j} V_{I-j}(y_k - a_{k,i,j}) + \sum_{i,j} W_{I-j}(y'_k - a_{k,i,j})\right\}. \quad (10)$$

Such an energy is computed as the spring ladder bypasses the isolated obstacle for an external force larger than the critical threshold that corresponds to the obstacle. The results of our adjustment have been reported as continuous lines in Figs. 2(b) and 2(c) for some obstacles situated in planes $(A1)$ and $(B1)$, respectively. It is worth noticing that in the ASC the internal energy U_{cell}, in addition to the interaction potential between the dislocation and the obstacle, also involves the elastic energy of the dislocation bowing. In the procedure of adjustment for the potentials V_{I-j} and W_{I-j}, the total line length has been chosen equal to the dislocation length L_x and the dissociation distance d_{SPD} and the spring stiffness γ were determined from Eqs. (4) and (7) with the proper L_y, i.e., corresponding to the cell of the ASC. Moreover the ASC and the ELM computations where performed with the same applied stress. In such conditions, and on the basis of the results shown in Figs. 7 and 8, we may expect that the ELM yields a satisfactory computation of the elastic energy contribution from the dislocation bowing.

In Figs. 10(a) and 10(f), we also present the ASC results and the corresponding ELM adjustments for the isolated obstacles situated in the next-nearest $(1\bar{1}1)$ planes, namely, (An) and (Bn) for $n \in [2,4]$. For the type I obstacles interaction with the trailing SPD, we found that a satisfactory description of the potentials could be obtained with some functions that are simply the symmetric of the interaction potentials with the leading SPD, i.e., $W_{I-j}(x) = V_{I-j}(-x)$. In order to specify the location of a type I obstacle, the subscript I is completed with the notation for the $(1\bar{1}1)$ plane where it is situated. For instance, a type I obstacle in the $(A3)$ plane will be referred as to an obstacle of type I-$A3$. From the comparison between Figs. 2(b), 2(c), and 10(a)–10(f), one notes that the interaction potentials, with multiple extrema when the obstacle is near the glide plane show only one extremum per SPD when the obstacle is situated further in the next-nearest planes, as it is expected from a Volterra elastic theory.[17,29]

C. Dimers pinning potentials

In previous studies bearing on the SSH in Ni(Al) system,[15,17] the role of clusters was put forward to explain the CRSS rate against c_s. Here we first examine the first-neighbor dimers which the interatomic bonds are oriented along either [110], [011] or $[10\bar{1}]$. The three configurations have been represented in Figs. 11(a)–11(c) and they are associated with three new types of obstacles, hereafter denoted by *type II*, *type III*, and *type IV*, respectively. Only the dimers situated either in $(A1)$ or in $(B1)$ planes are concerned. As done previously for type I, the interaction potentials that correspond to these obstacles are introduced in the ELM by fitting the ASC data obtained as described in Sec. II C. There are 12 new potential forms. For instance, the three potentials $V_{\text{II-}A1}$, $V_{\text{III-}A1}$, and $V_{\text{IV-}A1}$ concern the interactions between the leading partial and the dimers situated in the $(A1)$ plane whereas $W_{\text{II-}B1}$, $W_{\text{III-}B1}$, and $W_{\text{IV-}B1}$ are for the trailing partial and the dimers situated in the plane $(B1)$. The same procedure as for V_{I-j} and W_{I-j} is applied to derive these new interaction potentials. Replacing V_{I-j} and W_{I-j} in Eq. (1) and in Eq. (10) with V_t and W_t, where $t \in [\text{II-}A1, \text{III-}A1, \text{IV-}A1, \text{II-}B1, \text{III-}B1, \text{IV-}B1]$, the variation in the energy in the course of the spring ladder is computed for each type of dimer. The adjustment of the cubic polynomials associated with the different interaction potentials allows us to describe accurately the data obtained from ASC for U_{cell}, when an edge dislocation bypasses the different dimers. The energy variation computed from the ELM has been reported with continuous lines in Figs. 12(a)–12(f) for the dimers situated in the $(A1)$ plane and in Figs. 13(a)–13(f) for the dimers situated in the $(B1)$ plane. For comparison, the variations in U_{cell} obtained from ASC and targeted in the adjustment procedure have been represented in the same figures with symbols. Because of the asymmetry of the obstacles with respect to the X direction [see Figs. 11(a)–11(c)], the potential forms V_t and W_t have not the same symmetry as for V_{I-j} and W_{I-j}.

In addition to the previous dimers, parallel to the $(1\bar{1}1)$ planes we also consider some dimers, the bonds of which cross the glide plane. Figure 14(a) sketches out the formation of a first-neighbor dimer during the bypassing of a dislocation whereas Fig. 14(b) shows the opposite process, i.e., the dissociation of a pre-existing first-neighbor dimer. The variations in the potential energies associated with these processes are presented in Figs. 14(c)–14(f) for the two systems. The account of such dimers led us to the introduction of two new obstacle types in the ELM, denoted hereafter as *type V* and *type VI*. In Ni(Al), a marked variation in the potential energy, extending over the whole stacking-fault ribbon contributes to the dislocation pinning, being absent from or negligible in Al(Mg). This variation corresponds to an increase in the case of the formation of a first-neighbor dimer and to a decrease when a first-neighbor dimer is dissociated in the course of the dislocation passage. Such a variation has its physical origin in the fact that the order energy is much more important in Ni(Al) than in Al(Mg). With the interatomic potential used in the present study for Ni(Al), it was found that the formation energy for a first-neighbor dimer is 0.35 eV while it is −0.2 eV for the second-neighbor dimers. These formation energies were computed within independent ASC, i.e., with no dislocation inside the simulation cell. The potential-energy difference between the two configurations is then 0.55 eV which corresponds to the increase (respectively, decrease) in energy in Fig. 14(d) [respectively, Fig. 14(f)]. As the potential-energy rise extends over the entire staking fault, the mean force is close from 0.55 eV divided by the stacking-fault ribbon width, around 28 Å in our EAM model for Ni(Al), which would therefore give a pinning strength close from 0.03 nN. This is the same order as the maximum pinning forces reported in Fig. 2(a). In Al(Mg), the differ-

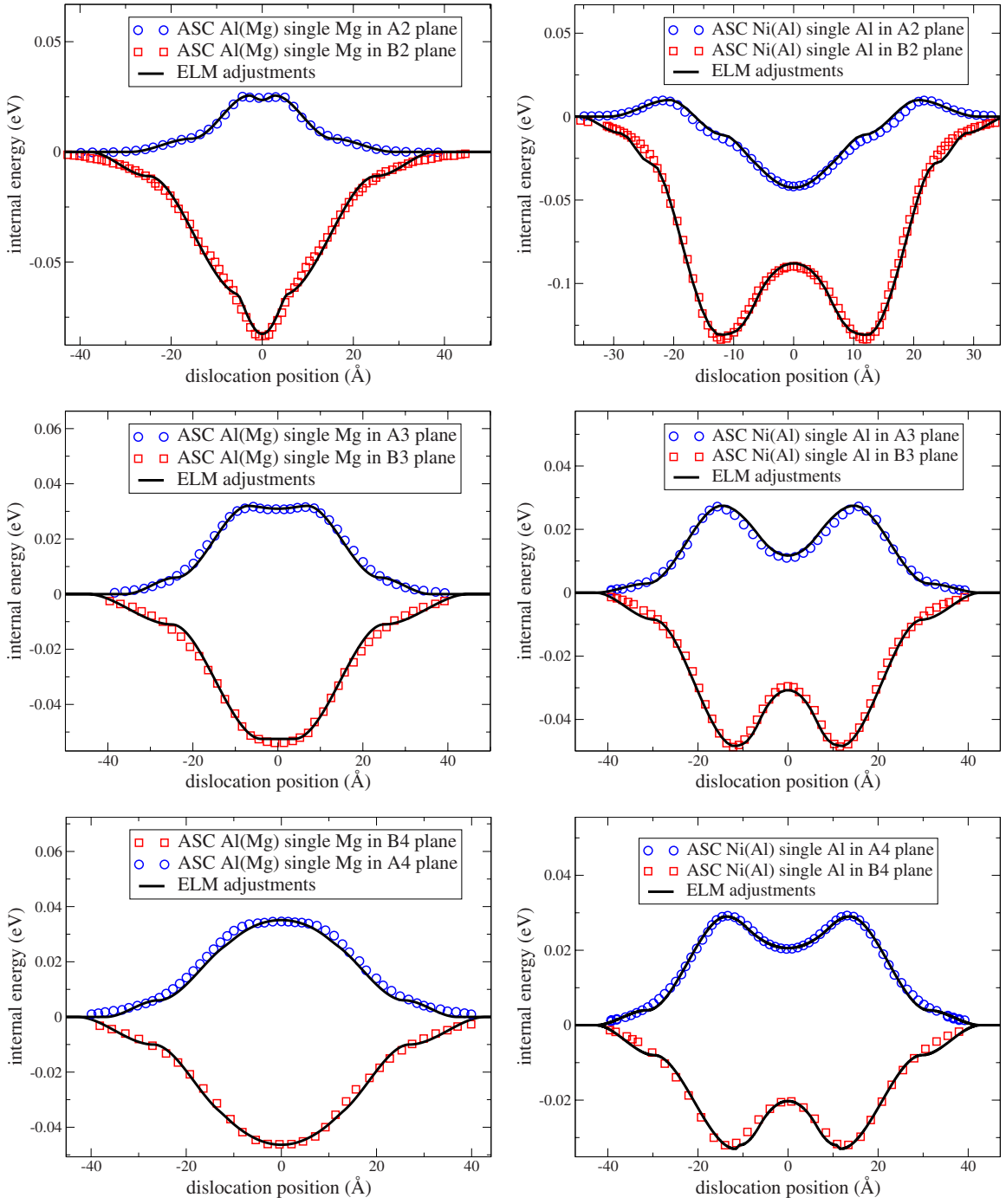

FIG. 10. (Color online) Internal energy of the simulation cell U_{cell} for an edge dislocation bypassing a type I obstacle situated in the nearest planes $(1\bar{1}1)$ above and below the glide plane. The planes are referred as a function of their apical height (see the text). The continuous lines have been obtained from the ELM, detailed in the text.

ence between the dimer formation energies is one order smaller as we found 0.03 eV in our EAM model for Al(Mg). Then, accordingly the associated pinning effect is negligible. In an earlier publication,[15] the large energy formation in Ni(Al) leads the authors to regard the type V and VI dimers as strong contributions to the dislocation pinning. On the basis of the present work, one will be able to answer the question raised in Ref. 15.

IV. DISLOCATION STATISTICS IN SRP SOLID SOLUTIONS

Here, first we must emphasize that the ELM parameters have been adjusted to fit the elementary interactions between the edge dislocation and the obstacles and that such an adjustment remains independent of the following statistical study, where no adjustable parameter is required. The random potential landscape of the elastic ladder is constructed

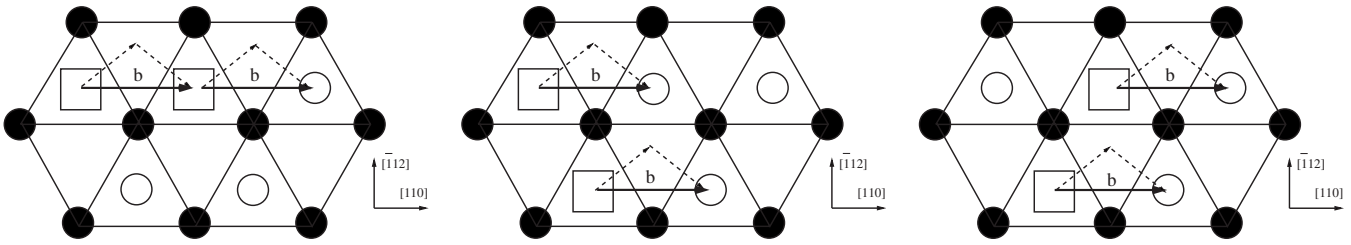

FIG. 11. Schematic representation for the first-neighbor dimer configurations in the $(1\bar{1}1)$ plane. Portion of the two nearest $(1\bar{1}1)$ planes that bound the dislocation glide plane. The square symbols correspond to the solute atoms whereas the circles represent crystal atoms. Open symbols represent atoms situated above the glide plane, the full symbols the ones below the glide plane. The arrows indicate the relative motion of the atom in the course of the dislocation passage.

by selecting randomly the sites of the hexagonal lattice [Fig. 6(a)] that are occupied by the obstacles. The distance d_g over which the elastic ladder is dragged, the total chain length L_x and the simulation cell size in Y direction, L_y have been chosen equal to those in the ASC in next sections (see Ref. 31). In ELM for SRP solid solutions, the total number of obstacles, distributed on the discrete lattice is $N_o = c_s L_x d_g / s$. Each site of the hexagonal lattice can take two possible states: (i) unoccupied or (ii) occupied by an obstacle of type I-$A1$. Then the nearest-neighbor sites of each occupied site are probed in order to recognize the dimers, i.e., the obstacles of type II, III, and IV [see Figs. 11(a)–11(c)], distinguished by the direction of their bonds. According to the bond direction, the type of obstacle is identified as either II-$A1$, III-$A1$, or IV-$A1$. Then one of the two sites concerned by the dimer is considered as bearing the obstacle with the suitable type and the other one is forced into the unoccupied state. This avoids the double counting of the dimer obstacles. The lattice sites can then take five different states.

The dynamical equation for the leading spring chain is extended to the case with multiple types of obstacle,

$$\lambda \dot{y}_k = \frac{\Gamma}{\sqrt{3}} \Delta_k y_k - \gamma [y_k - y'_k - 2d/b] + \tau s - \sum_{i,t} V'_{t-A1}(y_k - a^t_{k,i,A1}), \tag{11}$$

where now $a^t_{k,i,A1}$ is the Y coordinate of the ith obstacle of type $t \in [\mathrm{I}, \mathrm{II}, \mathrm{III}, \mathrm{IV}]$ in the kth row of the dimensionless hexagonal lattice, corresponding to the plane $(A1)$. The ELM predictions for the edge dislocation CRSS in the two different systems have been reported in Fig. 3 as continuous lines with open symbols. The excellent agreement between the ELM and the ASC demonstrates that the account of the different physical quantities, important in SSH, is correctly achieved. A quantitative agreement is obtained in both system Ni(Al) and Al(Mg) over the whole range of concentration. To determine the average critical shear stress, we used for every concentration a sampling of 20 configurations in ASC and 80 in the ELM where the computations are much shorter, i.e., few minutes each on a standard monoprocessor. The mean-square root of the CRSS dispersion computed from the ELM has been reported in Fig. 3 with error bars. The CRSS dispersion computed from ASC was found to be similar but less regular against c_s because of the limited sampling. From Fig. 3, one notes clearly that the CRSS dispersion increases with c_s in the two systems.

Switching off the dimer recognition in the ELM, the dimer-dislocation interaction then consists of the linear superimposition of the interaction between the two solute atoms and the dislocation. The critical CRSS has been computed in such a modified ELM in order to quantify the role of the dimers in the dislocation pinning. In Fig. 15, the results are compared with those obtained from the previous ELM, involving the potentials specific to dimers. For higher concentrations, above 4 at. %, the CRSS from the second ELM neatly deviates from the former model and becomes erroneous in comparison to the ASC reported in Fig. 3. In Ni(Al) the contribution specific to dimers enhances the CRSS while in Al(Mg), by contrast, it lowers it. In both systems, at $c_s = 10$ at. % the difference between the CRSS derived from the two different ELM may reach 15–20 % of the CRSS. In order to accurately approach the dislocation statistics, we are therefore compelled accounting for the pinning potentials of the dimers situated in the nearest $(1\bar{1}1)$ planes. The contribution of dimers proves though far much less important than what was expected from the analytical theory proposed in Ref. 17 by one of us (L.P.).

V. DISLOCATION STATISTICS IN TRP SOLID SOLUTIONS

To extend the ELM to the case of TRP solid solutions, we conserve the hexagonal lattice as presented in Fig. 6(a) and we describe the sites of the two $(1\bar{1}1)$ planes contiguous to the glide plane by a same single hexagonal lattice. This corresponds to the shift in the X direction presented in Fig. 6(a), which leads to superpose the two $(1\bar{1}1)$ planes. The total number of obstacles is fixed to $N_o = 2c_s L_x d_g / s$. Each site of the hexagonal lattice can take three different states: unoccupied, occupied by a type I-$A1$ obstacle or occupied by a type I-$B1$ obstacle. The dimers are then identified by probing the nearest-neighbor sites of an occupied lattice site, following the same procedure as in SRP (see Sec. IV). The ELM predictions for the pinning strength of TRP are shown in Fig. 4 and they demonstrate again a remarkable agreement with ASC. In the ELM, it is possible to cancel arbitrarily the recognition of type V and type VI obstacles. Then these solute atom dimers only contribute to the elastic ladder pinning

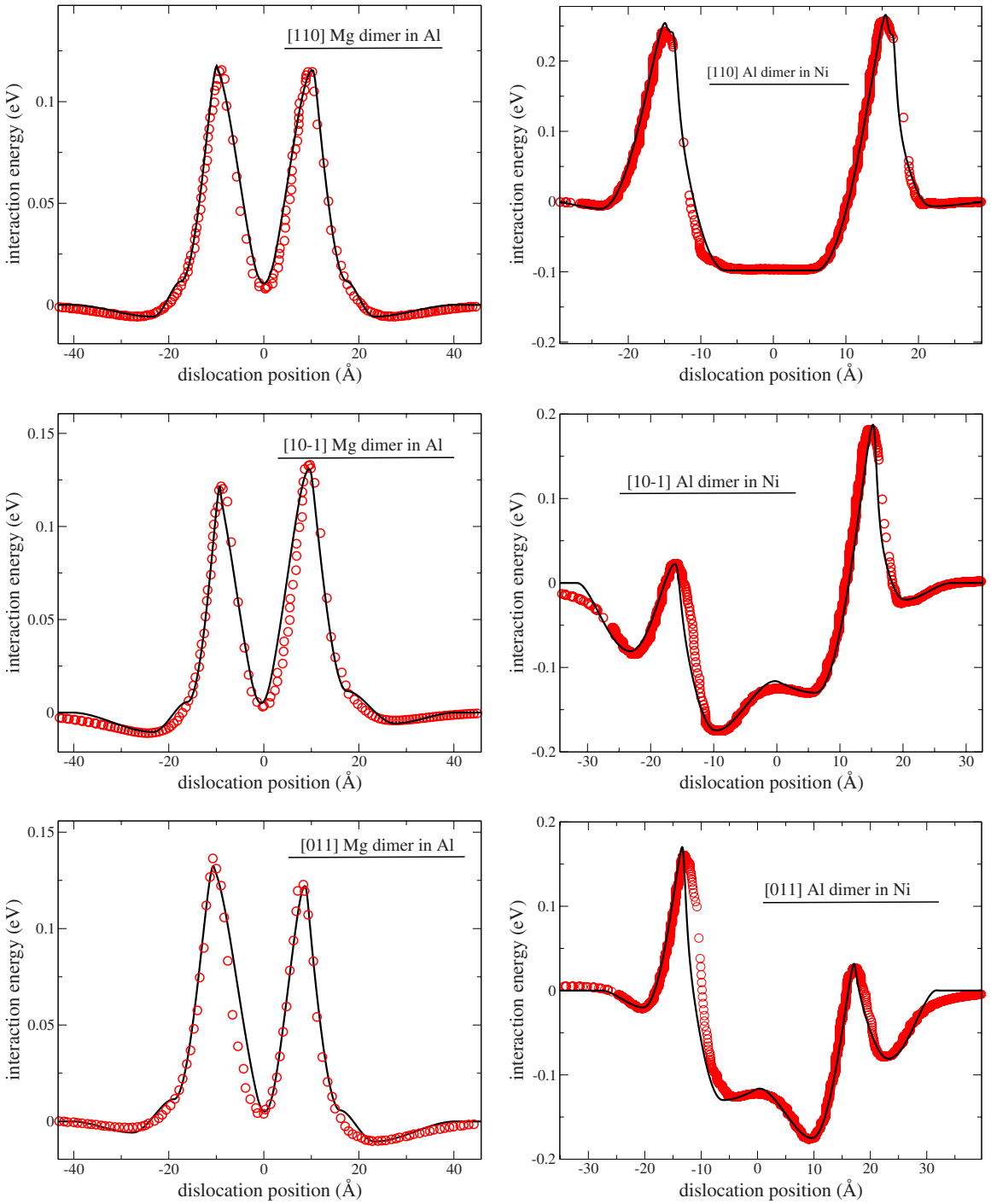

FIG. 12. (Color online) Internal energy U_{cell} in ASC for an edge dislocation bypassing dimers situated in the $(1\bar{1}1)$ planes just above the glide plane $(A1)$. On the left hand side Al(Mg) and on the right Ni(Al). Symbols represent the ASC data and the continuous line corresponds to ELM which the interaction potentials V_{i-n} and W_{i-n} $[i \in [\text{II},\text{III},\text{IV}]$ and $n=(A1)]$ have been properly adjusted on the atomistic data.

through the linear superimposition of the force fields due to the type I-$A1$ and I-$B1$ obstacles associated to form the dimer. With such a modified ELM, the computations for the TRP CRSS is presented in Fig. 16 for the two systems, along with the results obtained earlier with the original ELM, that is with specific potentials for type V and type VI obstacles. For concentration larger than 4 at. %, the account of these dimers may increase in more than 10% the CRSS in Ni(Al) and lowers it in Al(Mg). This reflects the same trend as for the type II, III, and IV obstacles in SRP (see Fig. 15). Such a comparison allows us to establish to which extent the larger order energy in Ni(Al) impacts the SSH in the ideal random solid solutions.

VI. DISLOCATION STATISTICS IN FRD SOLID SOLUTIONS

In addition to the pinning forces arising from the solute atoms situated in the two planes that bound the glide plane,

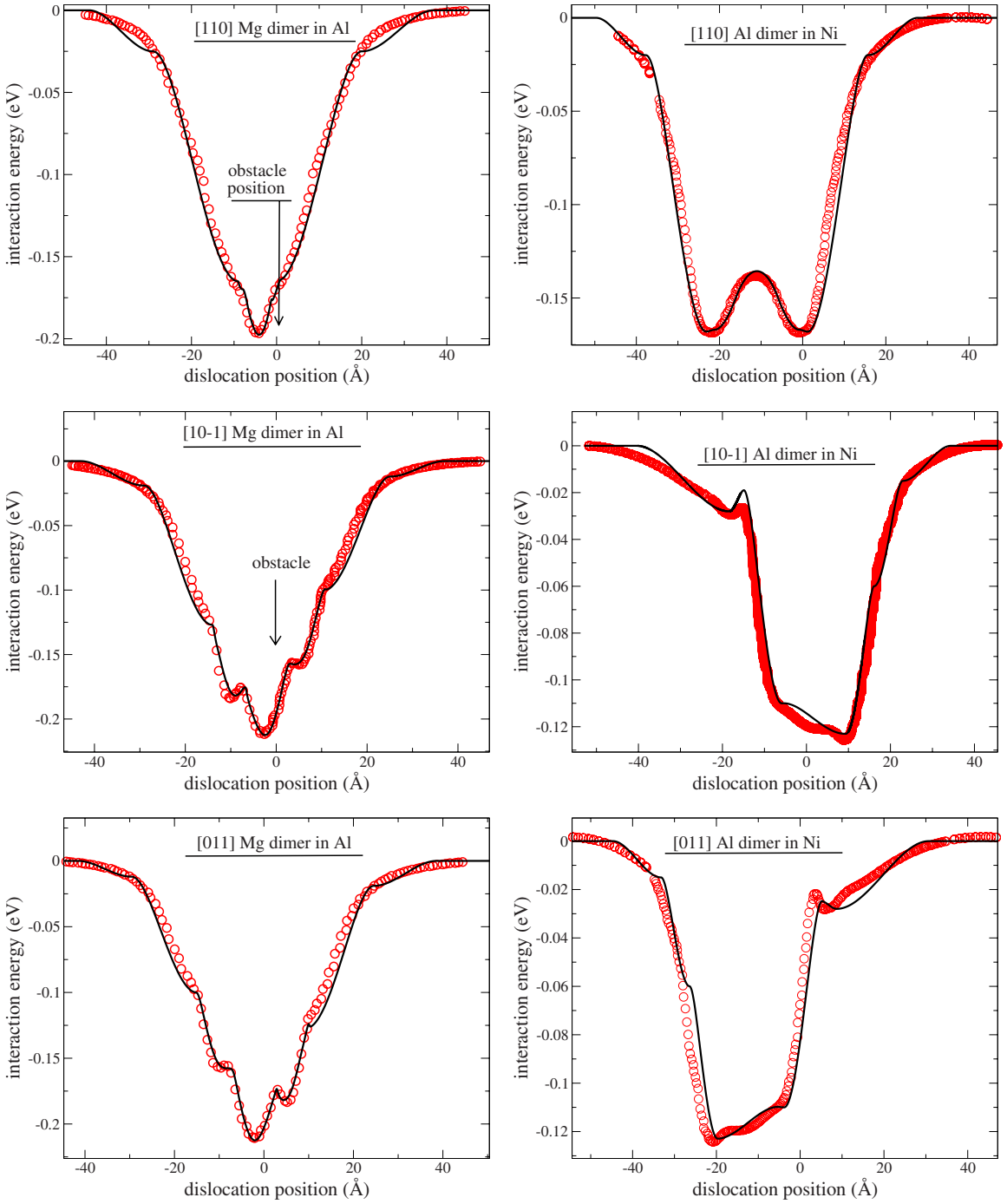

FIG. 13. (Color online) Same as in Figs. 12(a)–12(f) but for dimers situated in $(1\bar{1}1)$ planes just below the glide plane $j=(B1)$.

we now consider those situated in the next-nearest planes above and below, up to the fourth $(1\bar{1}1)$ planes, namely, (An) and (Bn) with $n \leq 4$ in our notations. It is equivalent to introducing a upper distance cutoff on the dislocation-obstacle interaction as earlier suggested by Nabarro in his analytical SSH theory.[2,40] We also studied the ELM statistics, including in our computations the contribution from further $(1\bar{1}1)$ planes, with $n \leq 7$, but no significant increase in the CRSS has been noticed in comparison to the case $n \leq 4$. This confirms Nabarro's assumption. In plane (An) and (Bn) with $n > 1$, i.e., further than the planes that bound the glide plane, we assume that the dislocation interaction with dimers and other clusters could be approximated as the linear superimposition of those with type I obstacles. This assumption proves satisfactory and allows us to limit the number of different types of obstacles that must be accounted for.

The total number of obstacles in the height nearest $(1\bar{1}1)$ planes is fixed to $N_o = 8c_s L_x d_g / s$. The obstacle recognition proceeds the same as for SRP and TRP (see Secs. IV and V). In Fig. 5, the CRSS computed for Al(Mg) and Ni(Al) is plotted against c_s. An excellent agreement is obtained between the ASC and the ELM predictions for the dislocation

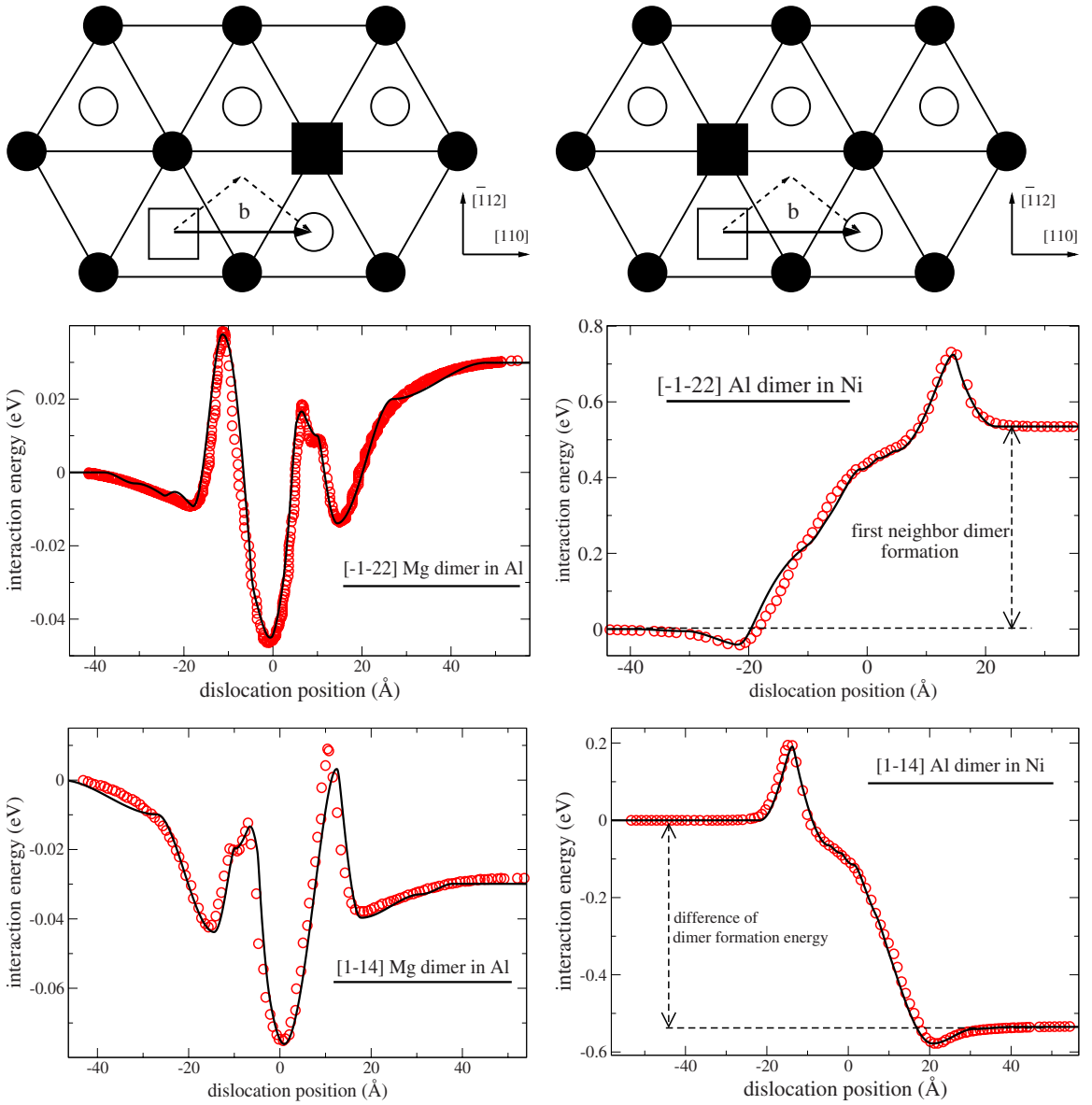

FIG. 14. (Color online) In (a) and (b), schematic representation of the solute atom relative flip for the dislocation bypassing some solute atom dimers which the bond crosses the glide plane (see legend in Fig. 11). The corresponding variation in U_{cell} computed from ASC are reported in (c) and (e) for Al(Mg) and in (d) and (f) for Ni(Al) as symbols. The continuous lines correspond to the ELM adjustments (see in text).

statistics in the two different systems. The ELM thus provides a satisfactory description of the edge dislocation statistics at the atomistic level. Such a result indicates clearly that the physical origin of SSH stems from a local interaction between solute atoms and the SPD.

In Fig. 5, we note that the scattering of the CRSS increases with solute content and even reaches same order as the CRSS itself, for c_s=10 at. %. Here the computations have been performed for a single dislocation. With an assembly of N independent dislocations the CRSS scattering can be expected to reduce by a factor $\sqrt{N}$, according to the central limit theorem. In macroscopic samples, this factor is much larger than unity which thence leads to a negligible CRSS scattering.

VII. MULTISCALE ELASTIC LINE MODEL

In Fig. 17, we reproduced the experimental data (open triangles), obtained by different authors through tensile tests,[24] applied to Al(Mg) monocrystalline samples. The low-temperature data have been treated such as to obtain the static depinning threshold,[3] avoiding strength loss due to the very low-temperature effects.[41] This strength loss, either due to the dislocation inertia,[42] to some quantum effects or to the weakness of the metal conductivity[43] must actually be ignored to properly evaluate the static depinning threshold. A mere extrapolation[3] of the experimental data from the temperature range where the stress-temperature rate is negative is expected to yield a satisfactory estimate for the static CRSS. Concerning Ni(Al), we did not found low-

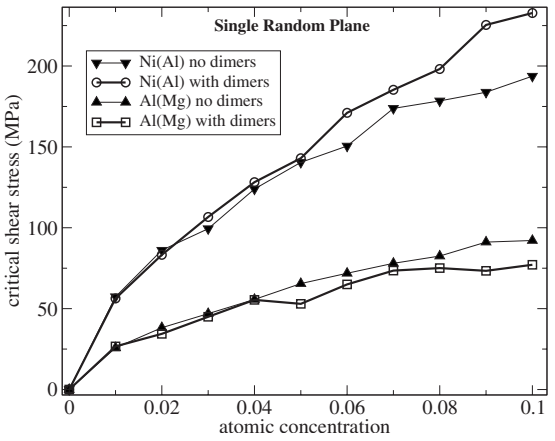

FIG. 15. Critical shear stress computed for Ni(Al) and Al(Mg) SRP solid solutions, within the ELM, as detailed in the text and sketched out in Fig. 6. The open symbols correspond to the same ELM as in Fig. 3. The full symbols correspond to the computations from an ELM where the solute atom dimers are approximated as the linear superimposition of the single solute atoms taking part to the dimers.

temperature tensile tests as for Al(Mg). We tentatively examined some experimental data from various sources as the deformation tests performed by Nembach and Neite[44] above 90 K, the compressive tests by Mishima *et al.*[45] above 73 K and the nanoindentations[46] measuring hardness (H), from which the yield stress σ can be deduced empirically by applying the linear relation $H=3\sigma$ (established for metallic crystalline materials[47,48]). However, those experimental data scatter too much and it has not been possible to extrapolate them against temperature in order to deduce the static CRSS. We thus choose to limit the comparison between our theoretical results and the experimental data to the Al(Mg) system.

The distance L_y has been chosen equal to 1 μm. For such L_y, $d_{\mathrm{SPD}}=d_0$ is a very good approximation. The total dislocation length has been fixed to $L_x=0.8$ μm, above which we found a CRSS invariant against L_x, indicating that the Larkin

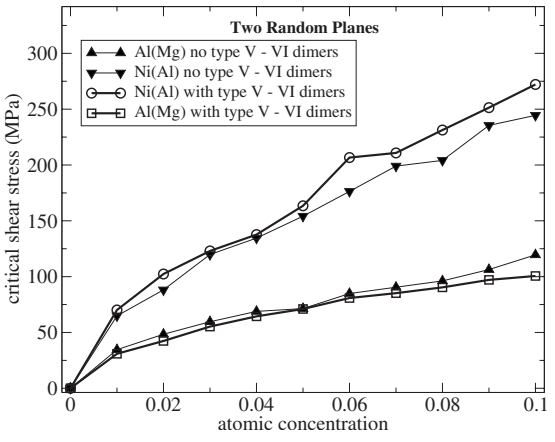

FIG. 16. Critical stress computed for Ni(Al) and Al(Mg) TRP solid solutions within ELM. The open symbols are the same as in Fig. 4. The full symbols correspond to a different ELM where type V and VI dimers are approximated as the linear superimposition of single solute atoms.

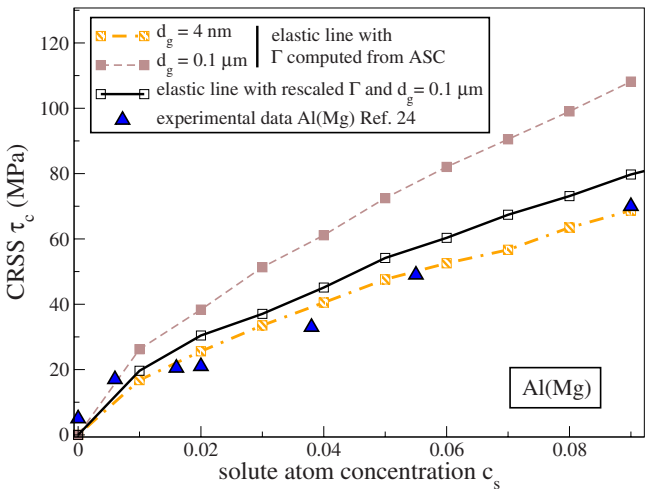

FIG. 17. (Color online) ELM computations for the CRSS against solute atomic concentration c_s in Al(Mg), for different glide distances d_g (see legend). For comparison, the experimental data from Ref. 24 for Al(Mg) were reported as triangles. The rescaling for the line tension Γ is detailed in the text.

length[33,49,50] is inferior to 0.8 μm. A series of ELM computations were performed with different glide distances d_g. In Fig. 17, the results are presented for Al(Mg) and they agree quite well with the experimental data, particularly for $d_g=4$ nm. Interestingly, we note that the CRSS increases with d_g. The CRSS dependence in d_g is the mere consequence of the increasing probability for the dislocation to encounter stronger obstacles in its course. This has been studied thoroughly in a simpler ELM (Refs. 33 and 51) where the CRSS was shown to increase with d_g as

$$\tau_c = A(c_s)\ln(d_g)^{\alpha}, \tag{12}$$

where A is a function of c_s and $\alpha<1$ is an exponent that varies linearly with $[-\ln(c_s)]$. With the present ELM, the parameter α has been adjusted such as to reproduce our numerical results (shown in Fig. 17) for $c_s=0.1$ in Al(Mg). It was found that $\alpha\approx 0.3$. The logarithmic variation in τ_c against d_g indicates that such a variation should be negligible in relative value for very large d_g.

In the present tentative to compare the theory with experiments, the distance L_y may be thought of as the shorter interdislocation distance, such that $L_y=\sqrt{1/\rho_d}$ where ρ_d corresponds to a realistic dislocation density in a weakly deformed alloy, i.e., $\rho_d\approx 10^{12}$ m^{-2}. The latter density leads to a typical interdislocation distance of 1 μm, corresponding to the one employed previously to compute the CRSS in Fig. 17. However, the dislocation density in the tensile tests is known to vary during the deformation process, which hinders a precise comparison between theory and experiments. In a same manner it is difficult to estimate d_g from the experimental works. Here we propose to integrate the Orowan relation between the deformation rate and the average dislocation velocity. It is then easy to show that $\epsilon=\rho_d b d_g$. With $\rho_d\approx 10^{12}$ m^{-2} and $d_g=100$ nm, we obtain $\epsilon=2.5\times 10^{-5}\%$, which proves far much smaller than the true elastic limit found in macroscopic tensile tests (see, for instance, Ref. 45)

Certainly, a manner to establish a more accurate comparison with experiments would be to work with data obtained from *in situ* studies where the glide of a single dislocation can be followed at low temperatures.[52–54] On the basis of the Orowan relation, a true elastic limit of few tenth of percent, more realistic in macroscopic tests, leads to d_g much longer than the ones used in our computations, reported in Fig. 17. However Eq. (12) yields a relative variation in the CRSS that becomes negligible for sufficiently large d_g. For instance, the same type of ELM computations as reported in Fig. 17 but for $d_g=0.5$ μm yields a CRSS only slightly larger than for $d_g=0.1$ μm. We therefore consider that the CRSS computed with $d_g=0.1$ μm is a good approximation for the CRSS in a macroscopic sample where d_g is expected to be much larger. Then the agreement between the theory and the experimental data reported in Fig. 17 is not very good since the computations overestimate the CRSS measurements in Al(Mg) by a factor 1.6. The agreement obtained for $d_g=4$ nm proved actually fortuitous results that is due to dimensional effects. The uncertainty of our computations might be put on the EAM employed to model the Al(Mg) interatomic forces. In Appendix A, a comparison between the different EAM is reported to computing the CRSS from ASC in Al(Mg). The EAM version proposed by Mendelev *et al.*[55] leads to a CRSS still larger than the one obtained with the EAM chosen in our study. Therefore we cannot expect that the change in EAM would solve the discrepancy, noticed between the experimental data and the theory.

The present work concerns the edge dislocations. Thence one may wonder whether the interplay of screw dislocation could explain our CRSS discrepancy. Since the transmission electron microscopy in the fcc alloys,[56] shows that the proportion of screw dislocations is similar to the edge ones, the screw depinning must occur for stresses comparable to the edge dislocations,[28] otherwise the microstructure of a deformed sample would imply a majority of edge dislocations. It seems therefore difficult to invoke the depinning of screw dislocations as a possible explanation for the theory failure.

We remark in Eq. (8) that according to the dislocation elastic theory the line tension Γ is expected to vary with the log of R, the outer cutoff radius. Such a quantity is usually related to the dislocation distance to nearest extended defects that can be a surface, a grain boundary or another dislocation. In theory, it is standard to assume that $R \propto \sqrt{1/\rho_d}$. Though, in our previous ELM application to microscopic scales we assumed that Γ could be kept equal to the value determined throughout our adjustment on the ASC dislocation profile (see Sec. III). In order to determine what Γ should be when $\rho_d \approx 10^{12}$ we assume that the logarithmic law for Γ, predicted by the dislocation elastic theory is verified but that the prefactor of such a law can be rescaled in order to match our computation for Γ at the atomic scale. Our additional assumption is equivalent to suppose that the ratio Γ/Γ^{el} is constant in the scale transition toward microscopic scales. With $R=\sqrt{1/\rho_d}/2$ we obtain a rescaled line tension $\Gamma=0.278$ nN instead of the $\Gamma_{Al}=0.101$ nN in Sec. III. Putting the new value for the line tension Γ in the ELM, the CRSS has been computed against the solute concentration for $d_g=0.1$ μm. The corresponding results are shown in Fig. 17 as a continuous line with open square symbols which now slightly overestimates the experimental data. According to our estimation the increase in Γ along the scale transition seems thus sufficient to resolve a large part of the theoretical discrepancy with the experiments.

For the sake of consistency between the different atomic-scale models, when we compared the dislocation statistics in ELM and ASC, i.e., in Sec. VI the stacking-fault energy γ_I in the ELM computations was fixed to the one computed in our ASC, i.e., within the EAM described in Sec. II. The ELM can also be employed independently from these EAM, in order to determine how the CRSS would vary with γ_I. According to the first-principles computations realized by Woodward *et al.*,[57] the separation distance between SPD is 8 Å for the edge dislocation in Al. In the EAM model employed here, we found $d_{SPD}=18$ Å. We thus correct in Eq. (4) the SFE in order to obtain $d_{SPD}=8$ Å in the ELM. This leads us to an SFE 2.5 larger than the one found in our EAM computations [see Eq. (5)]. We then performed the same ELM computations in Sec. VI but with the new value of SFE. It was found a CRSS of few percents smaller than those reported in Fig. 17. A strong SFE variation seems thus not to yield an important change in SSH.

A valuable property of ELM lies in that large samplings can be performed with a minimum of computational force, so that we obtain easily the CRSS with a very good precision. It is then of some interest to examine also the CRSS rate against c_s. Taking as targeted data the ELM results similar to those presented in Fig. 17, we adjust a power law of the form $\tau_c=Ac_s^{\eta}$, as it is predicted by different analytical theories for SSH.[1,2,4,5] In our fits of the ELM data in Fig. 17, the parameters A and η are adjusted on the different CRSS curves, corresponding to different d_g. We obtained: $\eta=0.61$ for $d_g=2.5$ nm and $\eta=0.67$ for $d_g=0.1$ μm. Clearly the effective concentration exponent η increases with the glide distance d_g,[51] a feature absent in the standard analytical SSH theories. It is however important to stress that the latter predict correctly that the CRSS decreases as the inverse of the line tension and that it increases with the maximum pinning force and with the solute content c_s. All these features are actually confirmed by our computations. On a pedagogical ground, the early SSH theories remain therefore highly valuable.

From our study of different simulation cell geometries, we also noticed that τ_c decreases with L_y when L_y is small enough to yield a separation distance d_{SPD} inferior to d_0. Such a decrease is the consequence of the staking-fault ribbon tightening, under the effect of the Coulomb-type interactions between the SPD and their periodic images in the Y direction. Actually the decrease in d_{SPD} with L_y [see Eq. (4)] leads to an increase in the spring constant γ in Eq. (7), which contributes to stiffer the ensemble of the elastic ladder and thus alters the total pinning strength. We exemplify the effect of a variation in L_y in the case of the random Ni(Al) solid solutions in Fig. 18. Here it appears neatly that for a small enough interdislocation distance L_y, the CRSS is inferior to the value computed for $L_y=1$ μm. In Al(Mg), for some geometries with small enough L_y, the computed values for the CRSS were comparable to the experimental data reported in Fig. 17 but such an agreement remains a fake yielded by the dimensional effect on L_y, which is then far too small in com-

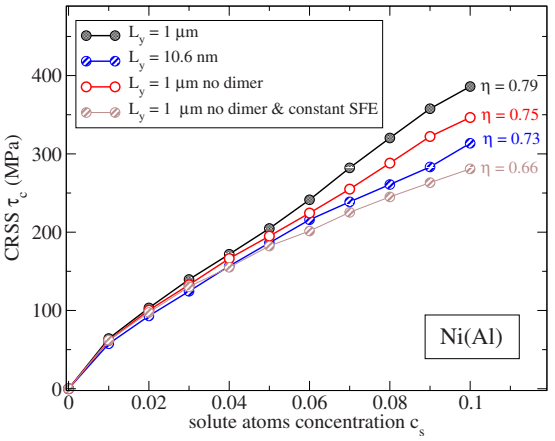

FIG. 18. (Color online) ELM computations for the CRSS against solute atomic concentration c_s in Ni(Al), for different distances between the dislocation periodic images along the Y direction L_y (see legend) and for different approximations for dimers interaction potentials and the SFE. The dislocation length is L_x =80 nm and the glide distance d_g=100 nm. The effective concentration exponent η is reported for each set of data.

parison with the realistic value of L_y=1 μm. The same type of fit in concentration power law as performed previously for Al(Mg) was realized in Ni(Al). Some of our results are reported in Fig. 18. For comparable dislocation geometries, L_x=80 nm, L_y=1 μm, and d_g=0.1 μm, the effective exponent η is found larger in Ni(Al) than in Al(Mg), i.e., η =0.79 in Ni(Al) against η=0.67 in Al(Mg). In order to confirm the importance of dimers in the pinning strength of FRD, as we noticed in SRP and TRP constrained solid solutions, we employ again the ELM where the dimer pinning potentials are approximated by the linear superimposition of the single solute atom ones. The results for the Ni(Al) FRD are presented in Fig. 18 where one notes that the ELM predictions deviate above c_s=4 at. % and that for c_s =10 at. % the linear approximation on the dimer potential underestimates by 10% the true predictions. Below c_s =4 at. % the SSH can be described in term of an interaction between the dislocation and the isolated solute atoms whereas above this concentration the account of the solute atom dimer is required in order to provide an accurate computation. The adjustment of an effective power law for the CRSS gives an exponent η=0.73 which is inferior to the value found in the ELM with specific dimer potentials (η =0.79) but which is still significantly larger than in Al(Mg) (η=0.67). In addition to the previous approximation on the solute atom dimers, we also performed some computations with the same ELM where the SFE is fixed to a constant, independent from c_s, that is the SFE computed in the pure Ni [see Eq. (5)]. The result for the CRSS is presented in Fig. 18 where one notices that the CRSS still decreases with the additional approximation. The reason for this is that fixing the SFE impedes the stacking fault ribbon to broaden with c_s, which according to Eq. (7) leads to a more rigid elastic ladder as it was analyzed previously about the CRSS variation against L_y. The adjustment of an effective power law gives an exponent η=0.66 which is, this time, comparable to the exponent found in Al(Mg) for the same geometry. We thus conclude that the difference in the CRSS rate between the two systems stems from the association of the dimer pinning strength with the variation in the SFE with the solute content.

VIII. DISCUSSION

Our analysis of the SSH in different model alloys, i.e., Ni(Al) and Al(Mg) showed that it is possible to obtain a quantitative agreement between ASCs and a suitably extended ELM. Our developments for ELM demonstrate how to transfer the data acquired at the atomic scale toward larger scales. On the basis of such a work, we believe that bridging ASC to multidislocations simulations as discrete dislocations dynamics[58] (DDD) could proceed through the development of a discrete version of ELM as the one presented here. We admit though that the work realized here is not yet sufficient to finalize an ASC to DDD bridging. Actually such a task would also require to account for the thermal activation of the dislocation glide as well as other processes as the solute diffusion and the dislocation cross slip. The integration of such mechanisms in ELM may be thought of as a long-standing work but it presents an encouraging perspective for a truly multiscale simulation.

A valuable property of the ELM lies in the fact that the different physical features introduced phenomenologically in the model can be switched off arbitrarily in order to determine their importance in the dislocation statistics and thence in SSH. Following such a scheme, the main contributions that differentiate hardening in Al(Mg) and Ni(Al) have been worked out whereas those of less importance could have been discarded, thereby leading us toward a consistent understanding of SSH. Here we demonstrated that the main contribution to SSH in fcc metals stems from the short-range interaction between the SPDs and the single isolated solutes situated in the nearest planes that bound the dislocation glide plane. In addition, the use of ELM allowed us to characterize the pinning contributions from (i) the solute atom obstacles situated in the vicinity of the glide plane, (ii) the solute atom dimers, and (iii) the effect of broadening of the stacking-fault ribbon. These features were found to be the physical ingredients needed in ELM to obtain a quantitative agreement with the dislocation statistics simulated through ASC. Noteworthy the Coulomb-type interaction between the solute atoms and the dislocation, stemming from the long-ranging dislocation stress field was discarded in the present version of ELM whereas it was integrated consistently in the ASC. The agreement obtained between the ELM and the ASC for the dislocation statistics shows us that the long-range interaction has a negligible weight in the determination of the CRSS, as it was early expected by Nabarro.[2,40] According to our computations, the pinning of solute atoms becomes ineffective when they are situated farther than the fourth-neighbor crystal planes from the glide plane.

Finally, it is worth stressing that qualitatively, the ELM is independent from the EAM model chosen to adjust its input parameters. Some atomistic data different than those derived from the present EAM can be used to adjust these parameters. For instance, the obstacle-dislocation interaction potentials and the dislocation elastic features could be derived

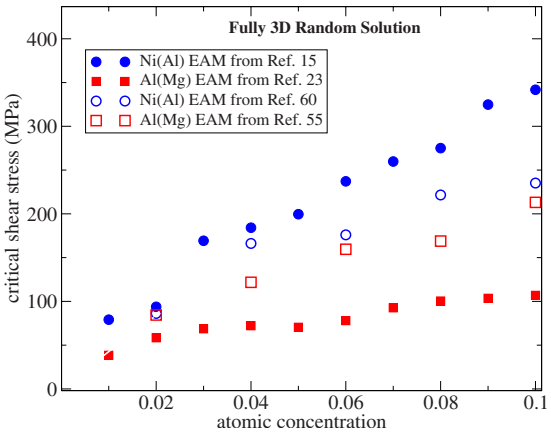

FIG. 19. (Color online) Critical resolved shear stress computed from ASC for the fully random solid solutions of Al(Mg) and Ni(Al) with different concentrations c_s and with the geometry given in Ref. 31. Different EAM are employed for the two systems (see legend). The EAM chosen for the present study are those developed by Liu *et al.* (Ref. 23) for Al(Mg) and by Rodary *et al.* (Ref. 15) for Ni(Al).

from different EAM interatomic potentials as those proposed by Mendelev *et al.*[55] and Purja Pun *et al.*[59] (see Appendix A) or else from some first principle studies. The important result of the present study was to show the feasibility of a quantitative agreement between the statistics of the ELM and the statistics of a dislocation in ASC. The comparison with the experimental tensile tests as exemplified with Al(Mg) (Ref. 24) in Sec. VII requires though to work further the multiscale approach.

APPENDIX A: COMPARISON OF SSH IN DIFFERENT EAM

For the same geometry of the simulation cell[31] as the ASC described in Sec. II F, the simulations are performed with different EAM to compute the CRSS in the fully random Al(Mg) and Ni(Al) solid solutions. The results obtained with the interatomic potentials employed in the present study, i.e., the EAM proposed by Liu *et al.*[23] for Al(Mg) and the EAM proposed by Rodary *et al.*[15] for Ni(Al) are compared with those obtained from the more recent EAM developed by different authors: the EAM proposed by Mendelev *et al.* in Ref. 55 for Al(Mg) and the one proposed in Ref. 59 for Ni(Al) by Purja Pun and Mishin. The different sets of data for the CRSS are presented in Fig. 19 where the results that correspond to the earlier EAM versions are the same as those already shown in Fig. 5. The comparison shows us that the CRSS computed from different EAM for a same system diverge which demonstrates the importance of the atomic-scale details into the SSH. With the recent EAM, the CRSS in the two systems are comparable. The choice to work with the EAM developed earlier in Refs. 15 and 23 was merely motivated by historical reasons since the present work started much before the publication of the recent EAM. Our study bearing essentially on the development of the ELM for the dislocation depinning statistics, the proper choice of an EAM potential is not the purpose of our study.

APPENDIX B: DISCRETE VERSION OF THE ELASTIC LINE MODEL

In the continuous version for the ELM, the athermal Langevin dynamics of the elastic body is given by the following equation:

$$BY_t(X,t) = \Gamma Y_{XX} - v'(Y) + f_A, \tag{B1}$$

where $Y(X,t)$ is the position of the string segment situated at the coordinate X, Γ is the stiffness of the line, f_A is the external applied force per unit length, $v(Y)$ is the random potential field per unit length, and B is a mobility coefficient. The single line model Eq. (B1) is extended to the case of two bound elastic lines. Then, the Langevin dynamics of the ensemble now composed with two strings is given by

$$BY_t(X,t) = \Gamma Y_{XX} - v'(Y) + f_A + g(Y - Y'),$$

$$BY'_t(X,t) = \Gamma Y'_{XX} - w'(Y') + f_A - g(Y - Y'), \tag{B2}$$

where $Y(X,t)$ [respectively, $Y'(X,t)$] is now the position of the leading (respectively, trailing) string segment and $v(Y)$ and $w(Y')$ are the random potential fields per unit length for the leading and the trailing lines. In Eq. (B2), we introduced the interaction force per unit length between the lines, denoted as $g(Y-Y')$. In the case of two partial dislocations, f_A stems from the Peach-Kohler force related to the applied stress τ. The component of such a force in the direction of motion is equal for both partials $f_A = \tau b/2$ where b is the total Burgers vector. In order to account for the atomic-scale details, Eq. (B2) must be discretized. To work with the hexagonal lattice, corresponding to the fcc $(1\bar{1}1)$ plane symmetry, we divide the dislocation line into segments of length $\mathcal{L} = \sqrt{3}b/2$ [see Fig. 6(a)]. The coordinate Y and X are rescaled: $y = 2Y/b$ and $x = 2X/\sqrt{3}b$. Multiplying Eq. (B2) by the elementary segment length $\mathcal{L}$, a new equation is obtained for the dimensionless dynamics of the leading string,

$$\lambda y_t(x,t) = \Gamma \frac{[y_{x+1} + y_{x-1} - 2y_x]}{\sqrt{3}} - V'(y) + \tau s + G(y - y'), \tag{B3}$$

where $s = \sqrt{3}b^2/4$, $V(y) = \mathcal{L}v(Y)$, $G(y) = \mathcal{L}g(Y)$, and $\lambda = sB$. The same equation holds for the trailing string with proper notations, switching the sign in front of G. The expression for the latter is derived in Sec. III.

[1] J. Friedel, *Dislocations* (Addison-Wesley, New York, 1964), p. 224.
[2] F. Nabarro, *Dislocations and Properties of Real Materials* (The Institute of Metals, London, 1985), p. 152.
[3] M. Z. Butt and P. Feltham, J. Mater. Sci. **28**, 2557 (1993).
[4] R. Labusch, Phys. Status Solidi **41**, 659 (1970).
[5] R. L. Fleischer and W. R. Hibbard, *The Relation Between te Structure and Mechanical Properties of Metals*, p. 261, HMSO, 1963.
[6] G. D'Anna, W. Benoit, and V. Vinokur, J. Appl. Phys. **82**, 5983 (1997).
[7] S. Zapperi and M. Zaiser, Mater. Sci. Eng., A **309–310**, 348 (2001).
[8] P. Moretti, M. Carmen-Miguel, M. Zaiser, and S. Zapperi, Phys. Rev. B **69**, 214103 (2004).
[9] R. Arsenault, S. Patu, and D. Esterling, Metall. Trans. A **20**, 1411 (1989).
[10] A. Foreman and M. Makin, Philos. Mag. **14**, 911 (1966).
[11] U. Kocks, A. Argon, and M. Ashby, *Thermodynamics and Kinetic of Slip* (Pergamon Press, Oxford, 1975), p. 60.
[12] M. S. Daw and M. I. Baskes, Phys. Rev. Lett. **50**, 1285 (1983).
[13] F. Ercolessi and J. B. Adams, Europhys. Lett. **26**, 583 (1994).
[14] J. Angelo, N. Moody, and M. Baskes, Modell. Simul. Mater. Sci. Eng. **3**, 289 (1995).
[15] E. Rodary, D. Rodney, L. Proville, Y. Bréchet, and G. Martin, Phys. Rev. B **70**, 054111 (2004).
[16] D. Olmsted, L. Hector, W. Curtin, and R. Clifton, Modell. Simul. Mater. Sci. Eng. **13**, 371 (2005).
[17] L. Proville, D. Rodney, Y. Bréchet, and G. Martin, Philos. Mag. **86**, 3893 (2006).
[18] K. Tapasa, D. Bacon, and Y. N. Osetsky, Mater. Sci. Eng., A **400–401**, 109 (2005).
[19] D. Bacon, Y. Osetsky, and D. Rodney, *Dislocations in Solids* (North-Holland, Amsterdam, 2009).
[20] S. Patinet and L. Proville, Phys. Rev. B **78**, 104109 (2008).
[21] R. Drautz, D. A. Murdick, D. Nguyen-Manh, X. Zhou, H. N. G. Wadley, and D. G. Pettifor, Phys. Rev. B **72**, 144105 (2005).
[22] M. I. Baskes, Phys. Rev. B **46**, 2727 (1992).
[23] X.-Y. Liu, P. P. Ohotnicky, J. B. Adams, C. L. Rohrer, and J. R. W. Hyland, Surf. Sci. **373**, 357 (1997).
[24] V. P. Podkuyko and V. V. Pustovalov, Cryogenics **18**, 589 (1978).
[25] X.-Y. Liu, J. B. Adams, F. Ercolessi, and J. Moriarty, Modell. Simul. Mater. Sci. Eng. **4**, 293 (1996).
[26] A. F. Voter and S. P. Chen, in *Characterization of Defects in Materials*, edited by R. W. Siegel, R. Sinclair, and J. R. Weertman, MRS Symposia Proceedings No. 82 (Materials Research Society, Pittsburgh, 1987), p. 175.
[27] D. Rodney and G. Martin, Phys. Rev. B **61**, 8714 (2000).
[28] S. Patinet and L. Proville (unpublished).
[29] J. Hirth and J. Lothe, *Theory of Dislocations* (Wiley Interscience, New York, 1982).
[30] D. Rodney and L. Proville, Phys. Rev. B **79**, 094108 (2009).
[31] L_x=69 Å and L_y=106 Å L_z=48 Å in Ni(Al), L_x=80 Å and L_y=120 Å L_y=56 Å in Al(Mg); the dislocation course is fixed to d_g=60 Å.
[32] M. Hiratani and V. Bulatov, Philos. Mag. Lett. **84**, 461 (2004).
[33] L. Proville, J. Stat. Phys. **137**, 717 (2009).
[34] J. Hirth and J. Lothe, *Theory of Dislocations* (Wiley Interscience, New York, 1982), p. 315.
[35] P. Heino, L. Perondi, K. Kaski, and E. Ristolainen, Phys. Rev. B **60**, 14625 (1999).
[36] H. Häkkinen, S. Mäkinen, and M. Manninen, Phys. Rev. B **41**, 12441 (1990).
[37] C. Carter and S. Holmes, Philos. Mag. **35**, 1161 (1977).
[38] K. Westmacott and R. Peck, Philos. Mag. **23**, 611 (1971).
[39] J. Hirth and J. Lothe, *Theory of Dislocations* (Wiley Interscience, New York, 1982), p. 180.
[40] F. Nabarro, Philos. Mag. **35**, 613 (1977).
[41] T. Parkhomenko and V. Pustovalov, Phys. Status Solidi A **74**, 11 (1982).
[42] R. Isaac and A. Granato, Phys. Rev. B **37**, 9278 (1988).
[43] Y. Estrin and L. Kubin, Scr. Metall. **14**, 1359 (1980).
[44] E. Nembach and G. Neite, Prog. Mater. Sci. **29**, 177 (1985).
[45] Y. Mishima, S. Ochiai, N. Hamao, M. Yodogawa, and T. Suzuki, Trans. Jpn. Inst. Met. **27**, 656 (1986).
[46] R. Cahn, Nature (London) **410**, 643 (2001).
[47] D. Tabor, *The Hardness of Metals* (Oxford University Press, New York, 1951).
[48] M. Y. Gutkin, I. Ovid'ko, and C. Pande, Philos. Mag. **84**, 847 (2004).
[49] A. Larkin, Sov. Phys. JETP **31**, 784 (1970).
[50] P. Chauve, T. Giamarchi, and P. LeDoussal, Phys. Rev. B **62**, 6241 (2000).
[51] L. Proville, Ann. Phys. **325**, 748 (2010).
[52] D. Caillard and J. Martin, *Thermally Activated Mechanisms of Crystal Plasticity* (Pergamon, New York, 2003).
[53] http://www.cemes.fr
[54] D. Caillard, Acta Mater. **58**, 3504 (2010).
[55] M. I. Mendelev, M. Asta, M. J. Rahman, and J. J. Hoyt, Philos. Mag. **89**, 3269 (2009).
[56] A. S. Argon, *Strengthening Mechanisms in Crystal Plasticity* (Oxford University Press, Oxford, New York, 2007).
[57] C. Woodward, D. R. Trinkle, L. G. Hector, and D. L. Olmsted, Phys. Rev. Lett. **100**, 045507 (2008).
[58] R. Madec, B. Devincre, L. Kubin, T. Hoc, and D. Rodney, Science **301**, 1879 (2003).
[59] G. P. Purja Pun and Y. Mishin, Philos. Mag. **89**, 3245 (2009).